ANISOTROPIC ELASTIC MODULI FOR CRYSTALLINE HEXAHYDRO-1,3,5-TRINITRO-1,3,5-TRIAZINE FROM MONTE CARLO CALCULATIONS

&

MOLECULAR DYNAMIC SIMULATIONS OF THE UNIMOLECULAR DISSOCIATION OF 1,3,3-TRINITROAZETIDINE

By

CARL MAHLON BENNETT

Bachelor of Science in Chemistry & Physics

Cameron University

Lawton, Oklahoma

1995

Submitted to the Faculty of the
Graduate College of the
Oklahoma State University
in partial fulfillment of
the requirements for
the Degree of
DOCTOR OF PHILOSOPHY
July, 2007

ANISOTROPIC ELASTIC MODULI FOR

CRYSTALLINE HEXAHYDRO-1,3,5-TRINITRO-1,3,5-

TRIAZINE FROM MONTE CARLO CALCULATIONS

&

MOLECULAR DYNAMIC SIMULATIONS OF THE

UNIMOLECULAR DISSOCIATION OF

1,3,3-TRINITROAZETIDINE

Dissertation Approved:

Lionel Raff

Neil Purdie

Mark Rockley

Ranga Komanduri

A. Gordon Emslie

Dean of the Graduate College

ACKNOWLEDGEMENTS

The engineering moduli work was conducted at Los Alamos National Laboratory, Los Alamos New Mexico under the direction of Dr. Tommy Sewell and in partial collaboration with T14 group during the summer of 1998. Acknowledgement and thanks is given to Dr. Donald Thompson for the Graduate Teaching Assistant and research opportunities during my full time at Oklahoma State from August 1995 to July 2001. Dr. Thompson has given me an improved ability to see the big picture and more importantly offered lessons that are beyond the scope of theoretical chemistry.

My Ph.D. advisor Dr. Lionel Raff deserves my deep gratitude and life long thanks for helping me through, not only my entire tenure at Oklahoma State University, but understanding and appreciating my goals and situation that has affected the beginning of my Ph.D. I am ready to get on the train. Thank you.

To my graduate professors and committee members; Dr. Paul Devlin for the motivation needed early on as a rookie graduate student when one realizes the insignificance of ones undergraduate successes as well as time talking of long motorcycle rides, Dr. Mark Rockley for the uncompromising professionalism in the lab where at any time is question and answer time, especially while holding undergraduate lab, and for the ever-so-probing questions during my qualification exam, Dr. Paul Westhaus for always spending the time with me explaining those difficult concepts, believing in “those chemistry students”, and not throwing those bits of chalk at me after repeating the

problem over and over, Dr. Nick Kotov for doubling my scientific library and giving me hope that a scatter brain can earn a Ph.D., Dr. Darrell Berlin for confidence and an old ear to get advise from, Dr. James Wickstead for not kicking me out of Electricity and Magnetism II after discovering I had not taken E & M I, Dr. Nick Materer for showing me how those experimental physical chemistry guys actually do things, Dr. Mario Rivera for conversation of analytical techniques and thought processes. All these professors are commended greatly for their professional and academic guidance and examples to me.

I cannot thank Drs.Yin Guo, Paras Agrawal and Dimitri Shalashalin enough for the hours spent mentoring and letting me bounce my sometimes crazy ideas off of them. I would like to thank all my fellow graduate student peers for motivation and academic support. Specifically; Carla Bartholomew, a great friend, who helped during the great migration from Cameron in 1995 with the Vet students, Lisa Phegley and James Graham who were the senior graduate students when I arrived that helped get me started, Teressa Sutton who showed me that graduate school can be hazardous to your health, Nevin Uras and Lisa Riley who were always right there in the trenches, and finally Justin Krouse for the unforgettable times in the lab and that final conversation with Dr. Raff that helped completed this journey.

Finally I would like to give thanks to my family for their constant support and encouragement during those trying times; my father and mother Gary and Dianne Bennett, sister Cheryl and brother-in-law Tony Rhodes, my wonderful children Molly, Carey and Maggie for which I focus on daily for inspiration and my fiancé, Cynthia for seeing me through the final chapter of this process for her love, patience and understanding.

All of the above, in addition to the hours upon hours of working in the lab, has molded my attitudes towards fundamental research, collaboration, academic methods, and life in general which I will in turn apply in my journey to contribute to the understanding and ongoing discovery of our great universe.

TABLE OF CONTENTS

LIST OF TABLES

Table Page

LIST OF FIGURES

PART ONE

CHAPTER I

INTRODUCTION

Stockpile Stewardship is the moniker used to describe ongoing reliability testing and maintenance without direct use and/or testing of the United States' nuclear stockpile. The majority of this Stockpile Stewardship is undertaken at the United States Department of Energy laboratories such as Los Alamos, Lawrence Livermore, Sandia laboratories and the Nevada Test Site. The high explosive materials used to condense a nuclear weapon's fissile material can degrade over time. These aged weapon components have many places where failure may occur. It is, therefore, important to conduct theoretical and indirect experiments on those chemical components and weapons systems to project and predict failure and longevity. Historically, there are substantial ripple successes from the initial reason for conducting this type of research. In the present work's case, methods have been developed that have applications well beyond Stockpile Stewardship. This work helps bridge atomistic methods to mesomechanical models.

Atomistic methods have been used to predict anisotropic elastic moduli; Young's and shear moduli, for hexahydro-1,3,5-trinitro-1,3,5-triazine (RDX). Again, the motivation for such a prediction stems from the need to develop incisive experimental

and theoretical tools capable of providing the fundamental physical and chemical behaviors of weapon components that must serve as the basis for improved "physics models" used to predict the safety, performance, and reliability of nuclear weapons all supportive to the Science Based Stockpile Stewardship. As the United States' nuclear stockpile ages and no new testing is conducted, methods must be developed to predict ageing effects. The possibility of physical and/or chemical ageing effects on individual components is increased as more and more systems remain in the stockpile beyond their designed service lifetimes.

The atomistic methods described here are used to predict the kinds of physical and mechanical properties required in the formulation and parameterization of detailed mesomechanics models. Mesomechanic models describe materials at the level of interacting constituents. For example, RDX is a component of a Plastic Bonded eXplosive (PBX). The PBX is composed of grains of an energetic material, RDX in this case, and held together by a polymeric binder. A mesomechanics model then describes the interaction between the polymeric binder and RDX. Each constituent must be characterized to such an extent that it may yield realistic results when incorporated into the model. This work describes those engineering constants that will contribute to the overall model in the characterization of the energetic material RDX.

As micromechanics models become more sophisticated, there is a need for more complete descriptions of the constituent properties. For example, specification of the Young's moduli, which describes the relationship between stress and strain in three orthogonal directions, rather than the isotropic bulk modulus or parameter values

spanning a domain of pressures and temperatures rather than a single point in *p*-*T* space may be required.

The remainder of this part is organized as follows: review of pertinent literature is given; methods used for the study are presented including; Isothermal-Isobaric Monte Carlo calculations, Potential Energy Surface, Strain, Fluctuations, Elastic Coefficients and Engineering Moduli; the section concludes with results, discussion, and conclusions.

PART ONE

CHAPTER II

REVIEW OF LITERATURE

Little work has been done specifically for this application, namely that of applying Monte Carlo data to calculate some set of engineering constants. The study of fluctuations and Monte Carlo as useful theories and tools is highly documented and used. This literature review shall focus on the following: work that has been accomplished within its scope since the publication of the work in Part One; Monte Carlo simulations as applied in some fashion with regard to determining engineering constants and/or parameters;

Work continues to characterize physical properties of weapons components. Bedrov *et al*[1] have studied polymorphs of octahydro-1,3,5,7-tetranitro-1,3,5,7-tetrazocine (HMX) using a quantum chemistry-based atomistic force field[2] to obtain unit cell parameters, coefficients of thermal expansion, and heats of sublimation. For the case of β-HMX polymorph anisotropic sound speeds were calculated from the molecular dynamics simulation-predicted elastic coefficients and compared with Impulsive Stimulated Light Scattering (ISLS) sound speed measurements where the level of agreement was found to be 'encouraging'. Theoretical computation of the structural and

molecular changes in 1,1-diamino-2,2-dinitroethylene (FOX-7) compressed to high pressures were investigated by Kuklja, Zerilli and Peiris[3] using *ab inito* calculations and the results compared to experimental data obtained from angle-dispersive X-ray diffraction analysis of the material compressed in a diamond anvil cell. These workers applied rigid, semi-rigid and complete molecular coordinate optimizations for comparison. Results indicated that although there is reasonable agreement for the rigid case, best agreement to experiment is found using the complete molecular coordinate optimization. The work herein describes a rigid molecule simulation cell where there is an over estimation of simulated crystal stiffness when compared to experiment[4]. This leads one to believe that there is certain significance on the removal of the flexible degree of freedom for the unit cell constituents.

The nine independent elastic constants of RDX were experimentally determined using resonant ultrasound spectroscopy by Schwarz *et al*[5]. The results were compared to this work as well as to that of the measured elastic constants of Haussühl[6]. Although the two measured sets of data[5,6] are in reasonable agreement (1.4% - 8.6%), the comparison to the current work is not as good. The computed values are up to two times that of experimentally measured. Again, this suggests that there is consequential significance to the rigid molecule simulation cell used in the current work.

Monte Carlo algorithms have been used in a number of engineering applications. Monte Carlo simulation techniques were used in a study of the tensile failure process of unidirectional T700 carbon-reinforced composite steel by Zhou *et al.*[7]. Monte Carlo was used specifically to allocate strength of the fiber elements and coupled with a stress analysis method. The technique proved very effective for understanding the tensile

failure process. In another study[8] MC simulation was used to support and predict elastic coefficients of bone and composite materials in comparison against acoustic immersion techniques. The study of bio-artificial tissues has included MC simulation to validate models that may predict strain factors of constituent materials[9].

Monte Carlo methods have a rich history[10] and have been used in a variety of fields. Methods specific to solving both classical and quantum mechanical problems are documented in the literature by Valleau and Torrie[11], Doll *et al.*[12] and Ceperley[13]. Certainly Monte Carlo has enriched and enabled the world of computational science and engineering. Doll and Freeman argue that MC occupies one of the top slots of the numerical algorithm chart[14].

PART ONE

CHAPTER III

METHODOLOGY

Isothermal-Isobaric Monte Carlo

For a system of N rigid molecules, the ensemble average of the macroscopic property $A(N,p,T)$, (p is pressure and T is temperature) is given by[15-17]

$$\left\langle A_{NpT} \right\rangle = \frac{\int d\mathrm{h} \int d\mathrm{s} \int d\Theta A(\mathrm{s},\Theta;V(\mathrm{h})) e^{-\beta\left[U_N(\mathrm{s},\Theta)+pV(\mathrm{h})-(N/\beta)\ln V(\mathrm{h})\right]}}{\int d\mathrm{h} \int d\mathrm{s} \int d\Theta e^{-\beta\left[U_N(\mathbf{s},\Theta)+pV(\mathbf{h})-(N/\beta)\ln V(\mathbf{h})\right]}}, \qquad \textbf{(1)}$$

where **s** and **Θ** are the molecular positions and orientations, respectively; U_N is the potential energy in terms of those variables; V is the volume; p is pressure; and $\beta=1/\kappa T$. The positions and orientations from Equation 1 are written in scaled coordinates, related to Cartesian coordinates **q** by the transformation **q=hs,** where **h** is the upper triangular matrix which transforms between the two coordinates systems. The columns of **h** are the lattice vectors **a**, **b** and **c**; the elements of **h**, therefore, specify the size, V=det(**h**) and shape of the volume under consideration.

The Monte Carlo estimate to Equation 1 is the arithmetic average of the microscopic function $A(\mathbf{s},\boldsymbol{\Theta};V)$, which is taken over the states of a Markov chain in the configuration space of the system,

$$A(N,p,T) = \lim_{M\to\infty} \frac{1}{M} \sum_{m=1}^{M} A(\mathbf{s}_m, \Theta_{\mathbf{m}}; V_m)\,, \tag{2}$$

where the transition matrix between successive states is based on the potential energies $U_N(s_{m,}\Theta_m)$ in such a way as to assure detail balance and equality of A(*N, p, T*) with the actual ensemble average given above. The independent variables are the 6*N* molecular positions and orientations plus the six nonzero elements of **h**.

The Markov chain is generated using a Metropolis algorithm[18] in which trial moves are accepted with the probability $P = \min[\exp(-\Delta),1]$, where, for the present state *m* and "trial" state *m*+1[15]

$$\Delta = \beta\left\{\left[U_N^{m+1} - U_N^m\right] + p\left[V^{m+1} - V^m\right]\right\} - N\ln\left(V^{m+1}/V^m\right). \tag{3}$$

Potential Energy Surface

The intermolecular potentials used are of the form[19],

$$U(\mathbf{R}) = \sum_A \sum_{B>A} \sum_{i\in A} \sum_{j\in B} \left[U_{rep}(\mathbf{R}_{ij}) + U_{disp}(\mathbf{R}_{ij}) + U_{elec}(\mathbf{R}_{ij})\right], \tag{4}$$

where *A* and *B* are molecules, and *i* and *j* denote particular atoms. The repulsion, dispersion and electrostatic terms are written as

$$U_{rep} = A_{ij} e^{-B_{ij} R_{ij}}\,, \tag{5}$$

$$U_{disp} = -C_{ij} / R_{ij}^6\,, \tag{6}$$

$$U_{elec} = q_i q_j / R_{ij}\,, \tag{7}$$

where *A, B, C* and *q* were taken from the work of Sorescu, Rice and Thompson[19]. The developed set of potential parameters was determined specifically for RDX by optimization of *A* and *C* for N-N and O-O. The parameters due to Williams and co-workers[20,21] were used for the remaining X-X repulsion and dispersion interactions. Partial charges were obtained from an electronic structure calculation for the RDX asymmetric unit (one molecule) in the gas phase. Parameters for X-Y interactions were defined using traditional combination rules. A parameter from a particular potential function of one molecule and/or atom is combined with the same type of potential but dissimilar molecule or atom in such a fashion where there is character contribution of each molecule or atom. These take on the explicit form of $a_{ij} = \sqrt{a_i a_j}$ and $b_{ij} = \left(b_i + b_j\right)/2$.

Although there are alternative functional forms and parameterizations for C, H, N and O in the literature[22-24] including one developed for flexible HMX[24], the set of repulsion and dispersion parameters due to Sorescu, Rice and Thompson[19] is the only one specifically calibrated for RDX. This set taken together with molecule and polymorph specific partial charges has been shown to be transferable to HMX polymorphs[25] as well as to a large set of additional nitramine containing molecular crystals. All potential parameters are provided in Reference 19.

Strain, Fluctuations, Elastic Coefficients and Engineering Moduli

In the theory of linear elasticity, the second-rank stress and strain tensors σ and ε are related through the elastic stiffness tensor **C** by[26]

$$\sigma_{ij} = C_{ijkl}\varepsilon_{kl} \qquad \textbf{(8)}$$

where *i, j, k, l* ∈ 1, 2, 3. The inverse of the stiffness tensor is known as the compliance tensor, $\mathbf{S} = \mathbf{C}^{-1}$.

Parrinello and Rahman[27] have shown that the fluctuations in the elastic strain provide a direct measure of the isothermal compliance for a general anisotropic medium through the relation

$$S_{ijkl} = \left\langle \varepsilon_{ij} \varepsilon_{kl} \right\rangle \frac{\langle V \rangle}{\kappa T}, \tag{9}$$

where $\langle V \rangle$ is the mean volume and $\left\langle \varepsilon_{ij} \varepsilon_{kl} \right\rangle$ is the outer product of the strain tensor with itself. The strain tensor ε is given by

$$\varepsilon = \frac{1}{2}\left(\mathbf{h_0'^{-1}} \mathbf{G} \mathbf{h_0^{-1}} - 1\right), \tag{10}$$

where $\mathbf{h_0}$ is the reference state of the system and $\mathbf{G=h'h}$ is the metric tensor. A prime (′) indicates a matrix transpose.

The compliance in Equation 9 is a fourth-rank tensor comprised of 81 elements. However, by taking advantage of the symmetry of ε, **S** can be rewritten in contracted, second rank form[28]

$$\mathbf{S} = \begin{pmatrix} \mathbf{M_1} & \mathbf{M_2} \\ \mathbf{M_3} & \mathbf{M_4} \end{pmatrix}, \tag{11}$$

where

$$\mathbf{M_1} = \begin{pmatrix} S_{1111} & S_{1122} & S_{1133} \\ S_{2211} & S_{2222} & S_{2233} \\ S_{3311} & S_{3322} & S_{3333} \end{pmatrix}, \tag{12}$$

$$\mathbf{M_2} = \begin{pmatrix} S_{1123} + S_{1132} & S_{1113} + S_{1131} & S_{1112} + S_{1121} \\ S_{2223} + S_{2232} & S_{2213} + S_{2231} & S_{2212} + S_{2221} \\ S_{3323} + S_{3332} & S_{3313} + S_{3331} & S_{3312} + S_{3321} \end{pmatrix} \tag{13}$$

$$\mathbf{M_3} = 2\begin{pmatrix} S_{2311} & S_{2322} & S_{2333} \\ S_{3111} & S_{3122} & S_{3133} \\ S_{1211} & S_{1222} & S_{1233} \end{pmatrix} \tag{14}$$

$$\mathbf{M_4} = 2\begin{pmatrix} S_{2323}+S_{2332} & S_{2313}+S_{2331} & S_{2312}+S_{2321} \\ S_{3123}+S_{3132} & S_{3113}+S_{3131} & S_{3112}+S_{3121} \\ S_{1223}+S_{1232} & S_{1213}+S_{1231} & S_{1212}+S_{1221} \end{pmatrix}. \tag{15}$$

For an orthotropic material, i.e. one in which the material properties are different in three mutually perpendicular directions, **S** assumes the form

$$\mathbf{S} = \begin{pmatrix} \mathbf{A} & \mathbf{0} \\ \mathbf{0} & \mathbf{B} \end{pmatrix}, \tag{16}$$

where

$$\mathbf{A} = \begin{pmatrix} 1/E_1 & \nu_{21}/E_2 & \nu_{31}/E_3 \\ \nu_{12}/E_1 & 1/E_2 & \nu_{32}/E_3 \\ \nu_{13}/E_1 & \nu_{23}/E_2 & 1/E_3 \end{pmatrix} \tag{17}$$

and

$$\mathbf{B} = \begin{pmatrix} 1/G_{23} & 0 & 0 \\ 0 & 1/G_{31} & 0 \\ 0 & 0 & 1/G_{12} \end{pmatrix} \tag{18}$$

contain the Young's moduli E_i and Poisson ratios ν_{ij}, and shear moduli G_{ij}, respectively.

Thus, the desired engineering coefficients may be obtained from an *NpT* Monte Carlo realization by calculation of the fluctuations of the strain tensor, expressed in terms of the instantaneous scaling matrix **h** and reference state $\mathbf{h_0}$ (defined as the element wise arithmetic mean of **h** determined from the Monte Carlo realization).

At room temperature and atmospheric pressure, RDX crystallizes in the orthorhombic space group Pbca with a = 13.182 Å, b = 11.574 Å, c = 10.709 Å and Z = 8 molecules per unit cell[29]. This number of molecules was included in the primary

simulation cell using the measured structure to define the molecular geometry and initial crystal structure. Periodic boundaries were used to simulate the infinite solid and all interactions between molecules having center of mass separations of 20 Å or less were included in the energy evaluations.

One Monte Carlo cycle was defined to consist of five attempted rotations and translations per molecule plus 20 attempted variations in the size and shape of the primary simulation cell. Maximum displacements were adjusted to yield approximately a 50% acceptance probability for each kind of move. A complete realization consisted of 500 rejected warm up cycles followed by a sequence of 10,000 production cycles where property data were taken. The final configuration from one realization was used as the initial configuration for the next. The thermodynamic states for two successive realizations were required to differ by at least either 60 K and 1.0 GPa or 30 K and 2.0 GPa.

Uncertainties reported herein for lattice parameters correspond to the standard deviation of the mean obtained from statistically independent sub-averages computed along the Markov chain. The battery of analyses described by Hald[30] was used to determine a suitable length for the coarse grained observations. Uncertainties for the moduli and Poisson ratios were obtained using a boot strap method[31] in which the 10,000 Monte Carlo observations of **h** for a given (p, T) state were sampled randomly with replacement in batches of 2,500 to obtain the compliance tensor assuming that the sample pool of observations is representative of the population. Mean values and variances of the elements of the compliance tensor were obtained on the basis of 100 of these "boot strap cycles." Finally the standard error propagation techniques were used to obtain

uncertainties for the elastic moduli and Poisson rations derived from the compliance tensor. The error bars obtained in this way were found to be relatively insensitive to the precise values chosen for the bootstrap parameters. In all cases, error bars correspond to one standard deviation.

PART I

CHAPTER IV

RESULTS AND DISCUSSION

Rigid molecule isothermal isobaric Monte Carlo realizations were performed for crystalline RDX in order to extract the isothermal compliance tensor and hence the anisotropic elastic engineering coefficients. A set of temperatures and hydrostatic pressures relevant to the development of improved mesomechanical descriptions of energetic materials under weak to moderate stress loading was considered. An additional benefit of the calculations is new pressure-volume-temperature (pVT) equation of state information. While the calculations described here were performed in the rigid molecule approximation, previous agreement[31] with experiment using a similar potential energy parameterization suggest that this is not too severe an approximation for the quantities discussed below. The calculated stiffness matrix for (p = 2.0 GPa, T = 276K) is given in Table I. Also included in Table I is the ratio C_{ij}/C_{11}. C_{11} is the largest element of **C** for the case considered. Since the matrix is symmetric only the upper half is shown. It is seen that the form expected for orthotropic materials is well satisfied (Equations 16-18). The forms of the stiffness and compliance tensors share the same symmetry and have zero elements in the same locations. Each of the elements that should be zero for an

orthotropic material is at most 5% of the smallest formally nonzero one and most of them are much smaller. Similar results were obtained for other pressures and temperatures.

The calculated elastic moduli are collected in Table II. Plots of the pressure dependence (T = 276K) and of the temperature dependence (p = 0.0GPa) are shown in Figures 1 and 2. The magnitudes of the Young's and shear moduli (E_i and G_{ij}) at zero pressure are reasonable for an organic molecular solid and are seen to increase dramatically with increasing hydrostatic pressure. This is expected due to the significant ~15% bulk compression that occurs at the highest pressures.[31, 32] Anisotropy among the moduli is evident, although not prominently so. In particular, E_3 and G_{31} are approximately 2/3 – 3/4 the values of the remaining Young's and shear moduli. The relative increases in the shear moduli with pressure are smaller that for the Young's moduli. The temperature dependence of the moduli is relatively weak (see Figure 2) and is near the limit of precision of the calculations. However in most cases, the moduli decrease with increasing temperature (see Table II).

The six Poisson rations (ν) are tabulated in Table III. The qualitative features of ν_{21} and ν_{13} are representative of there remaining four. The relative uncertainties for ν_{ij} are significantly larger than that for either E_i or G_{ij}, and the temperature dependence is not resolved in the present calculations. Different ν_{ij} apparently have distinct pressure dependencies including statistically significant non-monotonicities.

For an isotropic material the bulk modulus K is given by

$$K = \frac{E}{3(1-2\nu)} \qquad \textbf{(19)}$$

If, for the case T = 304 K and p = 0.0 GPa, we compute the arithmetic average of the Young's moduli and Poisson ratios to obtain isotropic values E = 20.2 GPa and ν = 0.22

then we predict a zero pressure bulk modulus of K = 12 GPa, in good agreement with the experimental value K_{expt} = 13.0 GPa due to Olinger, Roof and Cady.[32] The set of elastic constants for RDX has been measured[5,6]. The comparison between experiment and calculation (T = 304 K, p = 0.0 GPa) is favorable but not outstanding. The resulting anisotropic Young's and shear moduli are 130% and 116% of the respective experimental values; the average Poisson ratio is 80% of the experimental number. Although the elastic moduli predicted are somewhat larger than the experimental values this is evidently balanced by a smaller Poisson ratio to yield bulk modulus within 4% of experiment. The two experimental studies are both in reasonable agreement. A possible reason for this behavior may be due to the rigid molecule model used in the computations.

The pV equation of state for RDX has been measured (T = 295 K, 0 GPa $\leq p \leq$ 9.19 GPa).[31] A phase transition was identified above 4 GPa, but the structure of the high pressure polymorph has yet to be determined. The unit cell volumes are presented with lattice lengths for 25 uniformly spaced p-T pairs (0.0 GPa $\leq p \leq$ 4.0 GPa and 218 K $\leq T \leq$ 333K). The lattice angles never deviate significantly from 90º. The results, which are collected in Table IV, are sufficient to allow for prediction of linear and volumetric coefficients of isothermal compressibility of the p-T surface. Values for some of these are contained in Tables V where available experimental data are also reported. For purposes of comparison in the remainder of this section the calculated results were standardized to a temperature T = 295 K. Values corresponding to T = 295 K were obtained using least square fits of the lattice parameters as $f(T;p)$. In cases where

hydrostatic compression results are compared to experiment, the 0.05 GPa difference between the two is ignored.

The isothermal compression is in good agreement with the experimental data as seen in Table V. Specifically the percent errors in the calculated lattice lengths and unit cell volume at p=0.0 GPa are 1.6%, 1.3% and 0.3% for *a, b* and *c,* respectively and 3.1% for the unit cell volume. A comparison of the linear and volumetric compression x/x_o where x = *a, b, c,* or *V,* $x=x(p)$ and $x_o=x(p=0)$ along the T=295 K isotherm yields errors of -0.6%, 1.3% and 0.2% for the lattice lengths and 0.8% for the unit cell volume. Temperature effects on the hydrostatic compression are small for the temperature domain considered. The average percent difference in x/x_o for the two limiting temperature is only 0.3% and 1.1% for lattice lengths and unit cell volume, respectively.

TABLE I. Calculated stiffness matrix (GPa) and relative values C_{ij}/C_{11} for the case T = 276K, p = 2.0 GPa. Relative values are in parentheses in the bottom half of the matrix structure.

49.570	14.310	17.690	0.187	-0.215	-0.313
	44.291	16.417	-0.462	0.209	-0.188
(1.000)		40.162	-0.227	-0.380	-0.054
(0.289)	(0.894)		13.186	0.304	-0.235
(0.357)	(0.331)	(0.80)		9.754	-0.198
(0.004)	(-0.009)	(-0.005)	(0.266)		12.018
(-0.004)	(0.004)	(-0.008)	(0.006)	(0.197)	
(-0.006)	(-0.004)	(-0.001)	(-0.005)	(-0.004)	(0.242)

TABLE II. Computed and Experimental stiffness matrix (GPa), T = 304 K and ambient pressure.

26.90[a]/36.67[b]	1.38/6.27	1.67/5.68			
	25.67/24.10	9.17/6.32			
		21.64/17.70			
			11.99/8.40		
				2.72/5.30	
					7.68/7.60

[a] Component of the stiffness matrix as computed in this work.
[b] Experimental work of Haycraft *et al.*[4]

TABLE III. Calculated Young's (E) and shear moduli (G) as $f(p,T)$. Units are GPa. Uncertainties in the last digit are in parentheses.

T (K)	p (GPa)	E_1	E_2	E_3	G_{23}	G_{31}	G_{12}
218	0.0	27.3(8)	27.0(8)	17.4(4)	9.6(3)	6.0(2)	9.1(3)
	1.0	30.3(8)	33.1(9)	28.2(8)	13.0(3)	8.5(2)	11.8(4)
	2.0	39(1)	35(1)	31.0(8)	12.0(3)	9.5(3)	12.3(4)
	3.0	65(2)	63(2)	41(1)	20.7(5)	11.2(3)	21.3(6)
	4.0	72(2)	85(3)	71(2)	25.4(7)	19.0(5)	26.2(8)
247	0.0	26.0(7)	25.5(7)	16.6(4)	9.1(3)	5.5(2)	8.9(3)
	1.0	32.5(8)	33(1)	29.3(8)	12.9(4)	8.1(2)	12.0(4)
	2.0	38(1)	36(1)	28.8(8)	13.5(4)	9.3(3)	12.4(4)
	3.0	63(2)	59(2)	41(1)	19.7(6)	11.3(3)	20.6(6)
	4.0	70(2)	83(3)	62(2)	26.3(6)	17.1(5)	26.7(7)
276	0.0	24.8(8)	23.0(8)	16.9(5)	8.6(2)	5.7(2)	8.3(3)
	1.0	31.6(9)	32.3(8)	29.9(8)	13.0(4)	8.2(2)	11.3(3)
	2.0	40(1)	36(1)	30.6(9)	13.1(3)	9.7(3)	12.0(3)
	3.0	58(2)	56(1)	41(1)	18.8(5)	11.5(3)	18.3(5)
	4.0	77(2)	78(2)	64(2)	24.1(7)	16.8(5)	25.0(9)
304	0.0	24.2(7)	21.1(6)	15.4(4)	8.4(2)	5.3(2)	7.6(2)
	1.0	29.8(8)	32.1(9)	26.6(7)	12.7(4)	8.0(2)	11.6(4)
	2.0	36(1)	35(1)	29.7(8)	12.9(3)	9.5(3)	12.6(3)
	3.0	58(2)	56(2)	38(1)	19.0(6)	11.4(3)	19.3(7)
	4.0	70(2)	74(2)	57(2)	25.7(7)	17.2(5)	24.9(7)
333	0.0	22.2(7)	20.2(6)	14.3(4)	7.4(2)	5.1(1)	7.9(2)
	1.0	31.1(9)	32.1(9)	26.0(7)	11.7(3)	7.7(2)	10.7(3)
	2.0	41(1)	37(1)	31(1)	13.4(4)	9.9(3)	12.3(4)
	3.0	57(2)	54(2)	40(1)	18.4(5)	11.5(3)	18.5(5)
	4.0	70(2)	74(2)	56(2)	24.1(7)	16.5(4)	25.1(7)

TABLE IV. Calculated Poisson ratios as *f(p,T)*. Uncertainties in the last digit are in parentheses.

T (K)	*p* (GPa)	ν_{21}	ν_{31}	ν_{12}	ν_{32}	ν_{13}	ν_{23}
218	0.0	0.20(2)	0.17(2)	0.20(3)	0.19(2)	0.27(3)	0.30(3)
	1.0	0.24(3)	0.32(3)	0.22(3)	0.21(2)	0.34(3)	0.24(3)
	2.0	0.18(3)	0.27(2)	0.20(3)	0.29(3)	0.34(3)	0.33(3)
	3.0	0.22(3)	0.20(2)	0.22(3)	0.27(2)	0.31(3)	0.42(4)
	4.0	0.31(3)	0.25(3)	0.26(3)	0.25(3)	0.25(3)	0.31(3)
247	0.0	0.17(2)	0.20(2)	0.18(2)	0.19(2)	0.31(4)	0.29(3)
	1.0	0.23(3)	0.25(3)	0.23(3)	0.25(3)	0.28(3)	0.28(3)
	2.0	0.19(2)	0.29(3)	0.20(2)	0.28(2)	0.38(3)	0.35(3)
	3.0	0.21(2)	0.20(2)	0.22(3)	0.27(2)	0.31(3)	0.39(4)
	4.0	0.29(3)	0.26(3)	0.25(3)	0.22(3)	0.30(3)	0.29(3)
276	0.0	0.19(3)	0.15(2)	0.20(3)	0.22(2)	0.22(3)	0.30(3)
	1.0	0.25(3)	0.27(3)	0.24(3)	0.25(3)	0.28(3)	0.27(3)
	2.0	0.17(2)	0.28(3)	0.19(3)	0.28(3)	0.36(4)	0.33(3)
	3.0	0.21(3)	0.24(2)	0.22(3)	0.27(2)	0.33(3)	0.36(3)
	4.0	0.24(3)	0.22(3)	0.24(3)	0.28(3)	0.26(3)	0.34(4)
304	0.0	0.17(2)	0.16(2)	0.20(3)	0.22(3)	0.25(4)	0.30(4)
	1.0	0.25(3)	0.29(3)	0.23(3)	0.22(3)	0.33(3)	0.27(3)
	2.0	0.20(3)	0.32(3)	0.20(3)	0.28(3)	0.38(4)	0.33(4)
	3.0	0.17(2)	0.25(2)	0.18(2)	0.29(2)	0.38(4)	0.43(4)
	4.0	0.28(3)	0.24(3)	0.27(3)	0.28(3)	0.29(3)	0.36(3)
333	0.0	0.16(2)	0.18(2)	0.18(3)	0.20(2)	0.28(3)	0.28(3)
	1.0	0.23(3)	0.23(3)	0.23(3)	0.25(3)	0.28(3)	0.31(3)
	2.0	0.18(2)	0.26(3)	0.20(3)	0.28(3)	0.34(3)	0.34(3)
	3.0	0.20(2)	0.25(2)	0.21(3)	0.28(3)	0.35(3)	0.38(4)
	4.0	0.26(3)	0.27(2)	0.24(3)	0.25(2)	0.33(3)	0.33(3)

TABLE V. Calculated lattice lengths and unit cell volumes as *f(p, T)*. Uncertainties in the last digit are given in parentheses.

T (K)	*P* (GPa)	*a* (Å)	*b* (Å)	*c* (Å)	Volume (Å^3)
218	0.0	13.376(3)	11.715(2)	10.706(3)	1676.9(3)
	1.0	13.160(4)	11.529(1)	10.458(3)	1586.1(3)
	2.0	12.974(4)	11.365(2)	10.310(3)	1519.7(3)
	3.0	12.859(3)	11.255(1)	10.172(2)	1472.0(2)
	4.0	12.775(3)	11.203(1)	10.065(2)	1440.3(1)
247	0.0	13.389(3)	11.730(2)	10.720(4)	1682.9(3)
	1.0	13.166(3)	11.537(2)	10.462(3)	1588.6(3)
	2.0	12.979(5)	11.374(2)	10.314(3)	1522.1(3)
	3.0	12.866(3)	11.261(2)	10.175(2)	1473.9(2)
	4.0	12.774(3)	11.203(1)	10.076(2)	1441.7(1)
276	0.0	13.400(3)	11.741(2)	10.739(4)	1688.6(4)
	1.0	13.169(4)	11.545(2)	10.472(3)	1591.5(3)
	2.0	13.004(4)	11.382(2)	10.311(3)	1525.6(3)
	3.0	12.875(4)	11.268(2)	10.180(3)	1476.4(2)
	4.0	12.785(2)	11.203(1)	10.076(2)	1443.0(2)
304	0.0	13.410(3)	11.758(2)	10.756(4)	1694.8(4)
	1.0	13.176(5)	11.552(2)	10.483(4)	1594.8(3)
	2.0	12.994(5)	11.390(2)	10.324(4)	1527.5(3)
	3.0	12.873(4)	11.273(2)	10.190(3)	1478.2(2)
	4.0	12.790(3)	11.205(2)	10.083(3)	1444.6(2)
333	0.0	13.424(3)	11.775(2)	10.771(5)	1701.4(5)
	1.0	13.178(4)	11.562(2)	10.495(4)	1598.2(3)
	2.0	13.020(4)	11.395(2)	10.323(3)	1530.9(3)
	3.0	12.881(4)	11.280(2)	10.190(3)	1480.1(2)
	4.0	12.786(3)	11.210(1)	10.093(2)	1446.2(2)

TABLE VI. Illustrative parameters pertaining to isothermal compression.

	a (Å)		b (Å)		c (Å)		V (Å)	
p (GPa)	Calc.[a,b]	Expt.[a,c]	Calc.[a,b]	Expt.[a,c]	Calc.[a,b]	Expt.[a,c]	Calc.[a,b]	Expt.[a,c]
0.0	13.407	13.20	11.754	11.60	10.750	10.72	1693.0	1641.4

	a/a_0		b/b_0		c/c_0		V/V_0	
T (K)[d]	Calc.	Expt.[c]	Calc.	Expt.[c]	Calc.	Expt.[c]	Calc.	Expt.[c]
218	0.955	····	0.956	····	0.940	····	0.859	····
295	0.954	0.960	0.954	0.942	0.938	0.936	0.853	0.846
333	0.952	····	0.952	····	0.937	····	0.850	····

[a] T=295 K.
[b] Obtained from linear least squares fit.
[c] Reference 32.
[d] For a pressure of 4 GPa.

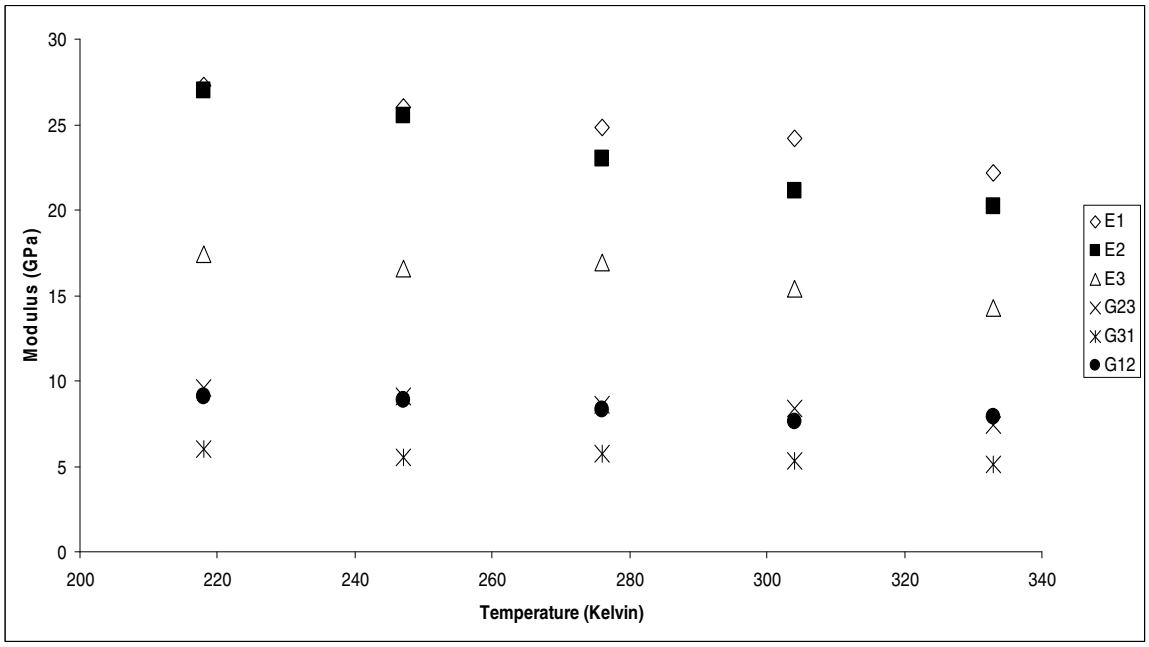

Figure 1. Young's and shear moluli for RDX are shown as a function of temperature for the fixed hydrostatic pressure of 0.0 GPa.

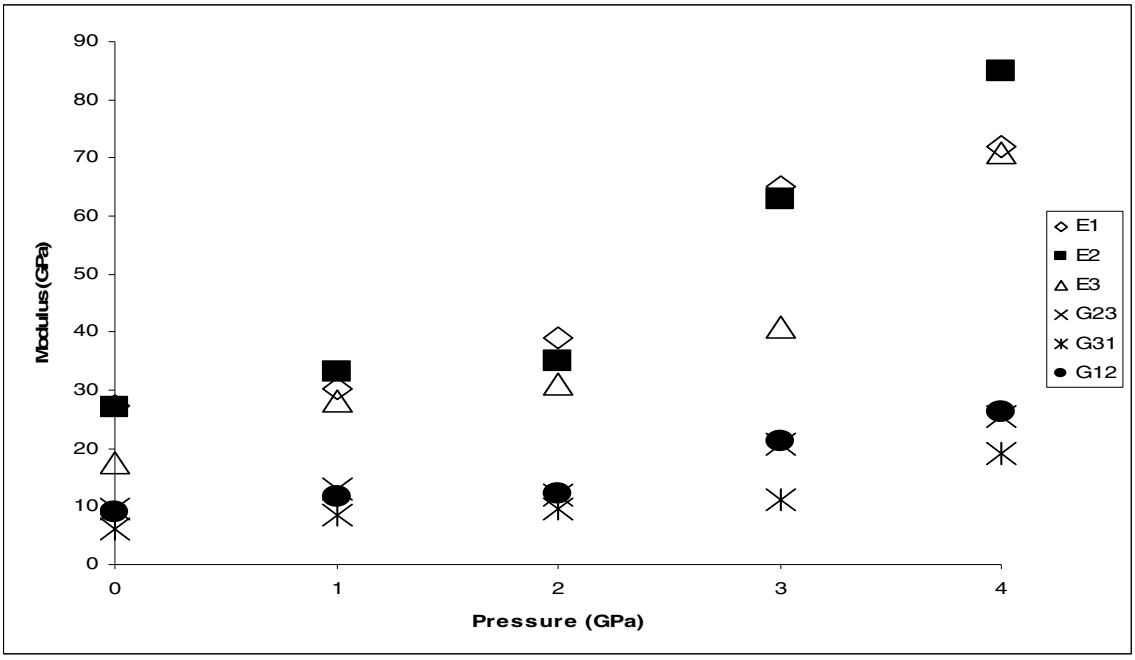

Figure 2. Young's and shear moluli for RDX are shown as a function of pressure for the fixed temperature of 276 K.

PART I

CHAPTER V

CONCLUSIONS

Isothermal-isobaric Monte Carlo calculations were used within an all-atom rigid-molecule framework to compute the elastic coefficient tensor C_{ijkl} and derived anisotropic engineering moduli and Poisson ratios for crystalline RDX as a function of temperature and hydrostatic pressure. The elastic coefficients were computed on the basis of formalism due to Parrinello and Rahman[27] in which the C_{ijk} are obtained in terms of fluctuations of the strain tensor. An additional product of the calculations is new *pVT* equation of state information from which quantities such as linear and volumetric coefficients of iso-thermal compression and thermal expansion can be obtained.

Assuming an orthotropic form for the compliance matrix, the Young's and shear moduli and Poisson ratio as a function of hydrostatic pressure and temperature in the domain 0 GPa $\leq p \leq$ 4 GPa and 218 K $\leq T \leq$ 333 K are obtained. The results for room temperature and pressure are in reasonable, though not outstanding, agreement with experimental determination of these quantities[5,6]. The moduli are predicted to increase significantly at higher pressures which is physically sensible given the ~15% compression that occurs at the upper end of the pressure domain considered.

The results indicate thermal "softening" of the crystal as the temperature is increased, although the extent of this softening is not monotonic with pressure, nor is it well resolved in all circumstances.

The calculated linear volumetric isothermal compression T = 275 K is in good agreement with experimental results with errors of 3% or less. The temperature dependence of these quantities is predicted to be small over the domain studied. Coefficients of Thermal Expansion (CTE) were computed[112] but not reported here. The error in linear CTE is 16, -49, and -35% for along the *a, b,* and *c* axes respectively. The error in volumetric CTE is over -35%. This discrepancy has also been noted by the developers of the potential set used and may arise in part due to the use of rigid molecules. There was a rather large pressure dependence of the CTEs ~ a factor of 3-5 in passing from p = 0 GPa to p = 4 GPa at constant temperature.

PART TWO

CHAPTER I

INTRODUCTION

One of the frontiers of theoretical molecular dynamics is the study of large polyatomic molecules, namely, those that have more that five atoms. Finding the exact quantum mechanical solution for such a system is not yet attainable due to, among other things, the accuracy of quantum theory and computational expense. As has been the case over the years, classical molecular dynamics is a practical alternative. The elucidation of the dynamics and mechanisms of polyatomic reactions will add to the knowledge of what is most important in chemistry, that is, the making and breaking of bonds. Recall also that a reactant will almost always dissociate into products via more than one channel and in more than one step. These facts motivated the present work.

The goal of this work was to develop a reactive potential energy surface that accurately models the decomposition of 1,3,3-trinitroazetidine (TNAZ). The dissociation of the NO_2 group through three reaction pathways has been considered where the results are compared to the experimental data of Zhang and Bauer[33]. In the process of this research, new questions and directions have presented themselves for future work, namely, intravibrational energy redistribution (IVR) in TNAZ. Additionally, due to the system's statistical nature, initial RRK correspondence is initially presented.

The reaction of interest is the unimolecular dissociation of TNAZ. It is widely accepted that cleavage of one of the NO_2 moieties is the first step in the decomposition of TNAZ. There are three possible NO_2 products; one from the N-N bond and two from the gem nitro-group leading to 1,3-dinitroazetidine and 3,3-dinitroazetidine products subsequently referred to as 13DNAZ and 33DNAZ, respectively in this work. Reaction 1 and 2 show the possible reaction paths. Figures 3, 4, and 5 show the general conformational structure of the reactant and major products. Notice that although only two paths are shown, three are available because the gem nitro's are not identical (see Figure 3). Therefore, two distinct reaction paths are available from the gem nitro-bond scission.

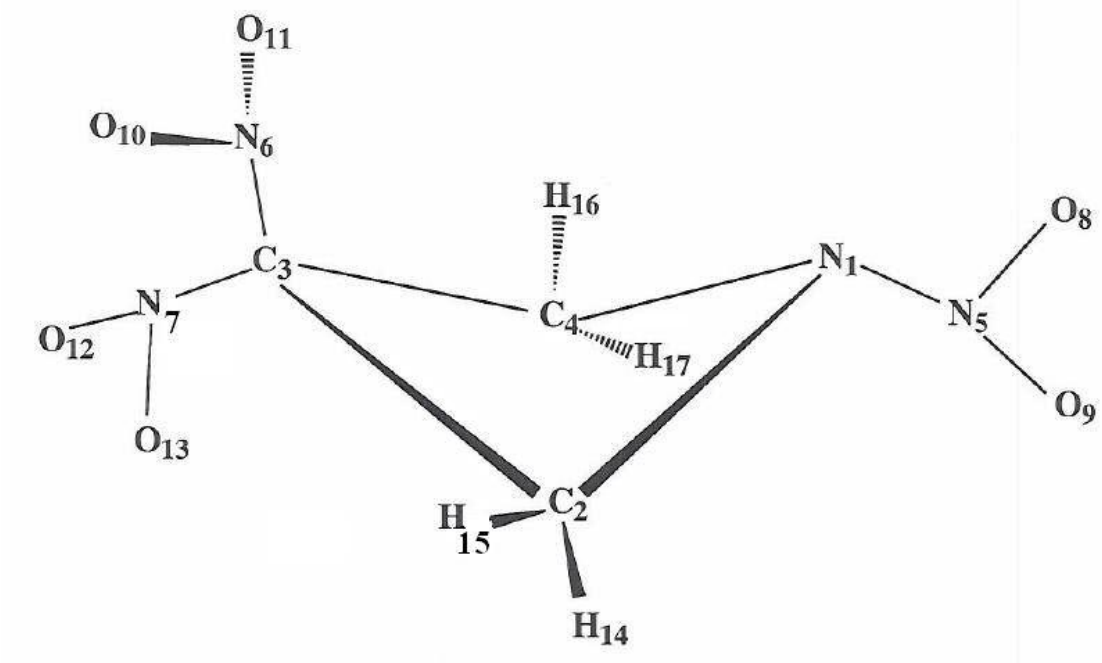

Figure 3. Dimensional projection and atom assignments for TNAZ.

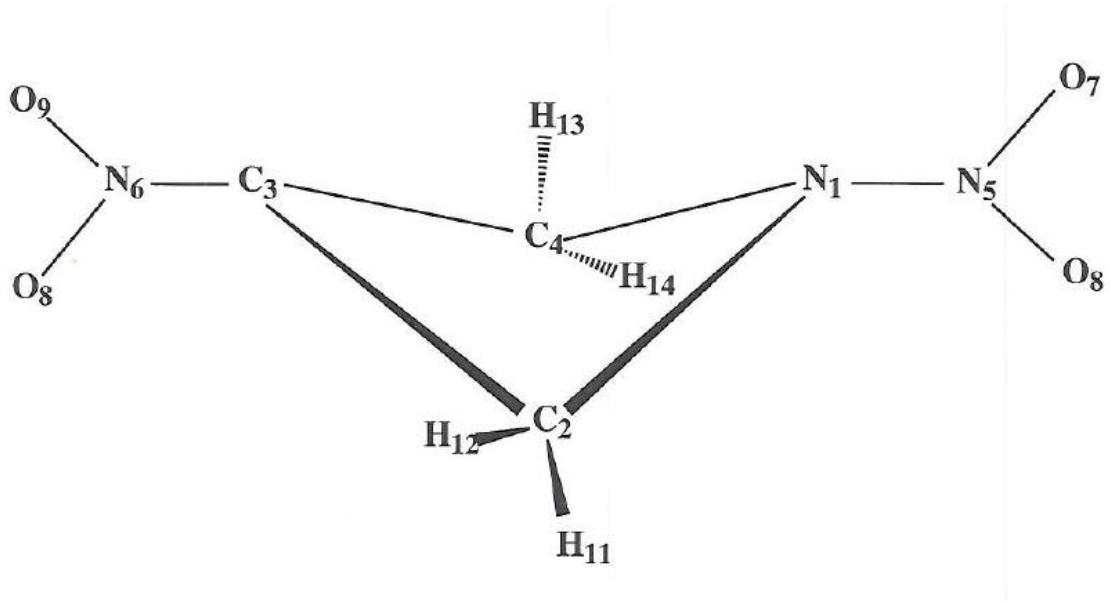

Figure 4. Dimensional projection and atom assignments for 13DNAZ.

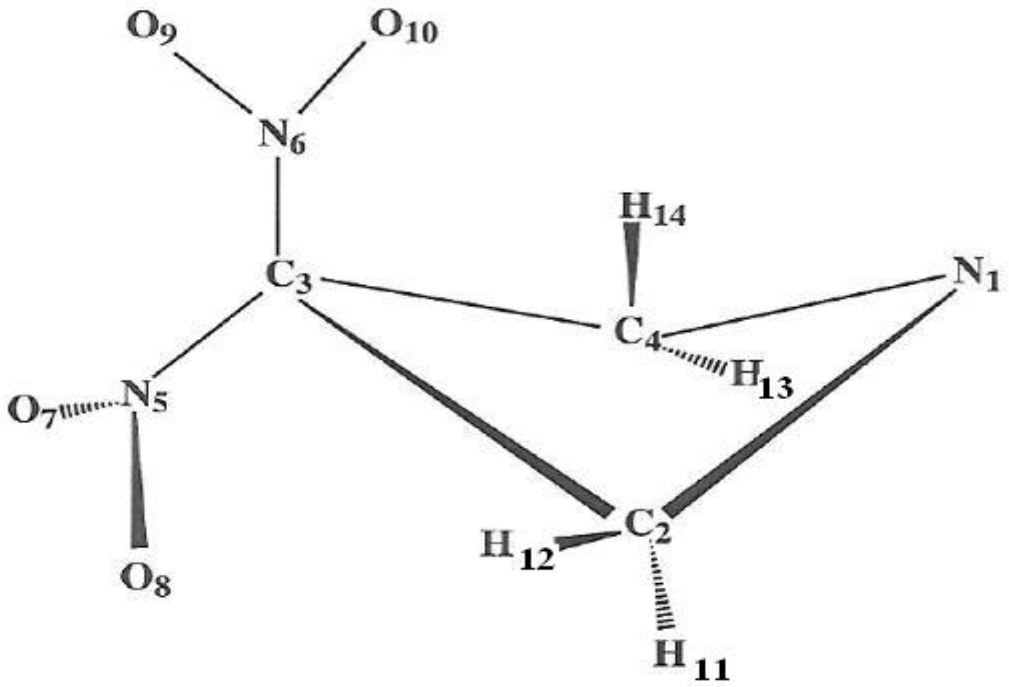

Figure 5. Dimensional projection and atom assignments for 33DNAZ.

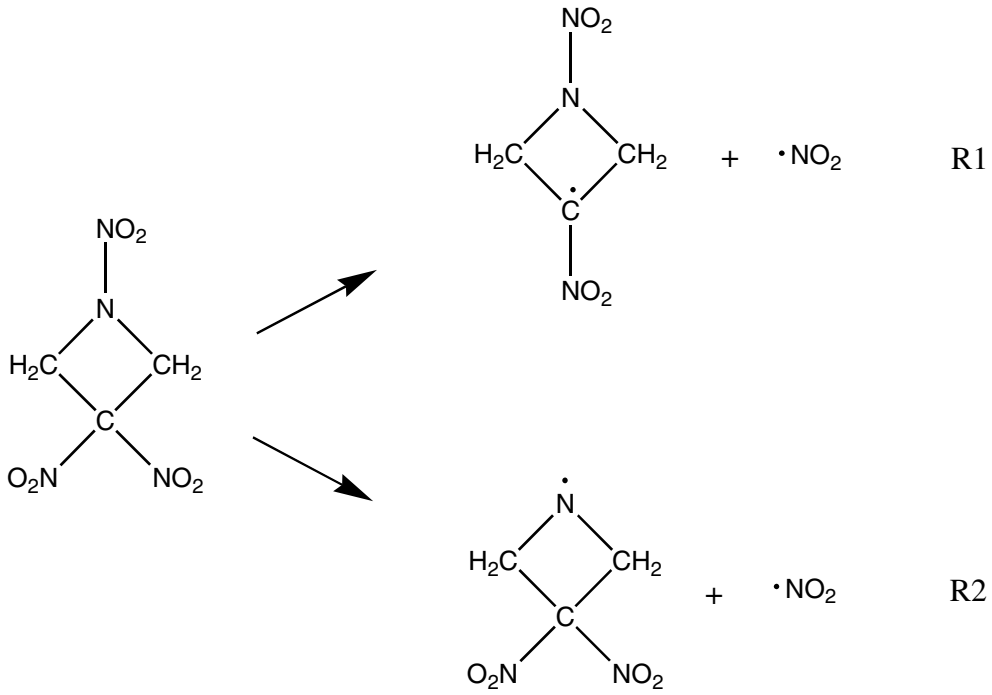

As can be seen from reaction R1 and R2, the products are all radicals. These products are undoubtedly short lived and will either combine with other products or further decompose. The reported experimental unimolecular rate constant found by Bauer[33] is

$$k = 10^{13.96\pm0.63}\exp\left[\left(-39.54\pm2.36\right)/RT\right]\mathrm{s}^{-1}$$

where the units of the gas constant R are kcal K^{-1} mol^{-1}. The reported experimental activation energy was determined to be 39.54 kcal/mol for temperatures in the range 700 K < T < 1100 K.

The remainder of this Part is organized as follows in Chapters. Chapter II is a review of pertinent literature. The key methods used in this work are presented in Chapter III. Results and discussion are given in Chapter IV. Conclusions and future work possibilities are recorded in Chapter V.

PART TWO

CHAPTER II

REVIEW OF LITERATURE

TNAZ is a relatively new energetic compound. It was first synthesized by Archibald *et al*.[34] in 1990. It is the smallest member of a class of cyclic nitramines with *geminal*-dinitroalkyl [C-$(NO_2)_2$] groups. TNAZ is considered to be one of the most powerful and least sensitive military explosives,[35] powerful in the sense that it provides a large amount of energy per mole upon detonation and insensitive in that TNAZ requires an initiation charge to induce a detonation reaction. These characteristics are of obvious value. A low weight explosive can possibly take fewer resources to fabricate and an insensitive explosive can be handled with less of a safety risk. TNAZ has the added, and favorable to production, quality of being steam-castable due to its low melting point of 374 K and thermal stability[36] up to 512 K. TNAZ is also a good candidate as a propellant as it produces a high number of moles per gram reacted. With regard to the experiments conducted to study the decomposition of TNAZ, information about its thermal stability can be derived from slow thermal heating and information about the initial decomposition steps is gained from rapid heating, high laser fluence and shock tube experiments.

The following literature review is divided into sections corresponding to specific subjects of research. First, the experimental work concerned with the structure and vibrational analysis is presented. Next, experiments that have used slow thermal heating to induce decomposition are discussed followed by fast heating experiments, which include rapid thermal heating, high laser fluence and shock tube experiments. Lastly, theoretical investigations are reviewed that include structural characterization, thermodynamical calculations, vibrational analysis and modeling of decomposition. The final paragraphs discus the common conclusions and discrepancies on the dissociation of TNAZ and how they apply to the present work.

Structure and Vibrational Analysis

Crowder and McKenney[37] have obtained an infrared spectra for solid TNAZ and acetyl-3,3-dinitroazetidine (ADNAZ) and made normal mode calculations to study the conformational changes in mixtures of 50/50 and 97.5/2.5 mole percent TNAZ/ADNAZ. TNAZ has been found to exhibit polmorphisms when in the form of a neat crystal or combined with some other material.[38] No frequencies below 500 cm^{-1} are reported. They conclude that one possible reason for the conformational change is a low barrier to rotation of the NO_2 groups as is seen in nitromethane[39] and nitroethane.[40]

Thompson *et al.*[41] have studied the vibrational spectra of matrix isolated TNAZ and compared with quantum chemical calculations. The experimental work was used to assign 24 of the 45 fundamental molecular vibrations. Hartree-Fock, second-order Moller-Plesset theory and three density functional theory methods were compared. Salient findings are that the DFT approach, namely the B3LYP[42] method, gives a more

accurate vibrational description than the other methods studied. The 24 experimental frequencies are shown in Table XVII.

Gas-phase FTIR spectra of TNAZ has been experimentally recorded by Yu *et al.*[43] as a tool along with calculated ΔH_F and some structural parameters to define thermochemical parameters of TNAZ for temperatures up to 1500 K and to estimate the equilibrium distribution of products generated during high temperature pyrolysis of TNAZ. Thermodynamic properties such as constant pressure heat capacity, entropy and the change in free energy are reported. They have taken the FTIR spectrum of TNAZ in the gas phase highly diluted in Ar at a resolution of 0.25 cm^{-1} where 39 of the 45 frequencies have been assigned. The frequencies are shown in Table XXI and are used as the basis for the ground-state force-field normal mode frequencies for TNAZ.

Slow Thermal Heating

The thermal decomposition pathways of TNAZ were found neat and in solution by Oxley *et al*. using high pressure liquid chromatography.[44] Thermolyses were performed isothermally in the range 160-280 °C. The neat samples of TNAZ contained between 0.2 and 0.3 mg. After thermolysis, the fraction remaining was assessed by dissolving samples in acetone or methanol and analyzing by liquid chromatography and tandem mass spectrometry. Neat TNAZ at all temperatures has been observed to decompose according to first-order kinetics out to 90% decomposition. Arrhenius parameters were determined using rate constants for at least four temperatures. The activation energy found is 46.6 kcal/mol, which is similar to that of pure nitramines[45] and the Arrhenius parameter found is 3.55×10^{17} s^{-1}. The shock tube experiments of Bauer[33] most approximate the high pressure limit and, therefore, differ from the neat and solution

experimental results of Oxley[44] *et al*. Through the use of isotopically labeled samples of TNAZ (TNAZd4) and deuterated solvents (protonic and benzene), the deuterium kinetic isotope effect (DKIE) was studied, and it was found that there is no intermolecular DKIE and a small intramolecular DKIE. The intramolecular DKIE for protonic solvents (acetone and methanol) was evident thru the 2 – 4 fold enhanced rate. For TNAZd4 the small DKIE reported, 1.31 for neat experiments and 1.38 for benzene indicate there is no primary DKIE effect for the unimolecular reaction of TNAZ. It is possible that there is a secondary DKIE where the C-D bond could contribute to the dissociation through perturbing the vibrational partition functions. The concluded decomposition pathways for TNAZ are one N-NO_2 bond homolysis or one C-NO_2 cleavage. They have found that N-NO_2 is slightly favored. At 10% decomposition 66% of bond homolysis is N-NO_2. TNAZ has been found to be more thermally stable than any of the 3,3-dinitroazetidium salts studied. At a scan rate of 20 °C/min the exothermic maximum occurs at 278 °C.

Anderson, Homsey, Behrens and Bulusu have studied the mechanism and reaction kinetics of the thermal decomposition of isotopically labeled TNAZ using a simultaneous thermogravimetric modulated beam mass spectrometer (STMBMS).[46] The thermolysis occurred isothermally at 10 °C increments spanning 160-210 °C. Gas products were collimated by two beam-defining orifices and a toothed wheel. Ions were generated in the mass spectrometer by electron impact at about 20 eV, which is less than the typical 70 eV. This was done to lessen the effect of ion fragmentation. Four routes of decomposition have been proposed. The principle step is nitramine bond cleavage (Reaction 1) and of significantly less importance at the *geminal*-dinitro site. Also significant is the nitro-nitrite rearrangement. All of these paths can create NO which

subsequently may directly displace the N-NO_2 groups on the remaining TNAZ. The elimination of HONO/HNO_2 has been found to be unimportant in the decomposition. 1-nitroso-3,3-dinitroazetidine (NDNAZ) has been found to be less thermally stable than TNAZ. Their reaction scheme is shown below.

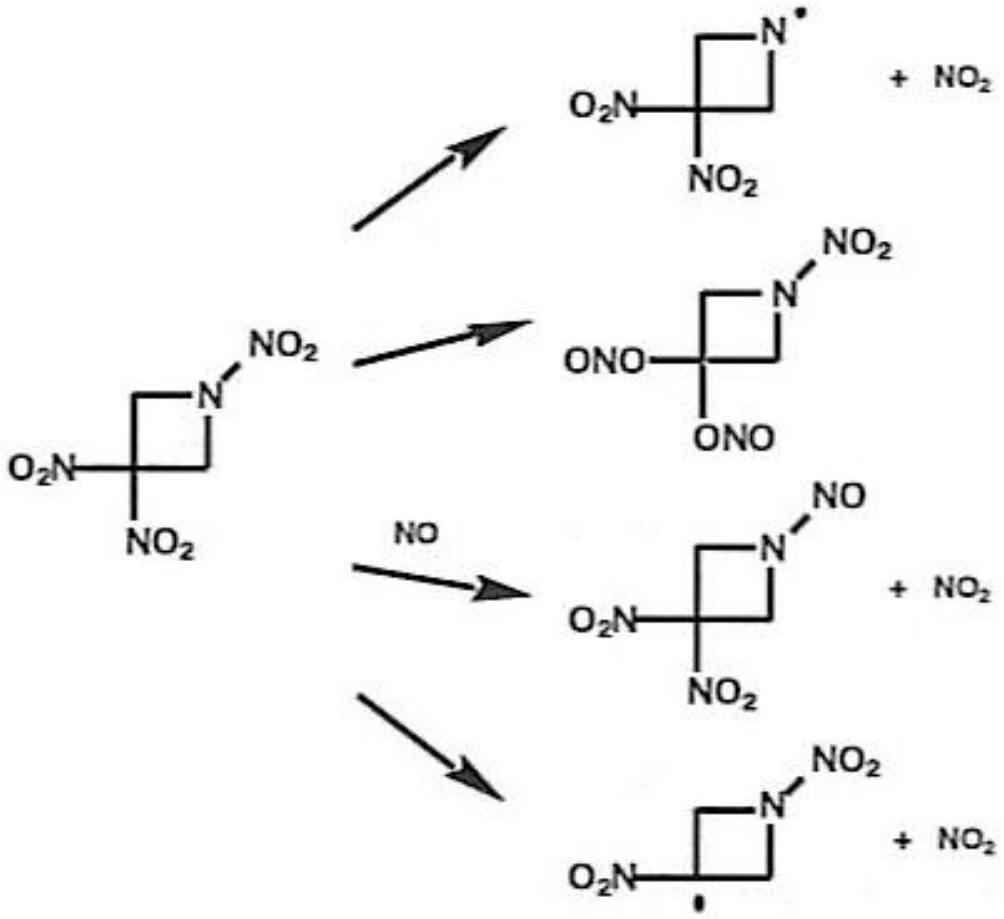

Bulusu and Behrens[47] have written a review article focused on the understanding of the complex physiochemical processes involved in the combustion and decomposition of RDX, HMX and other closely related cyclic nitramines including TNAZ using techniques such as STMBMS, time-of-flight velocity spectra analysis, isotope labeling, isotope scrambling techniques and DKIE effects.[48-53] The major products formed from

TNAZ decomposition have been found to be NO_2, NO, H_2O, HCN, CO/N_2, CO_2 and NDNAZ. The study has shown that, in common with RDX and HMX, the nitroso analogue, NDNAZ, plays an important role as an intermediate in the decomposition of TNAZ. Their results indicate that the rate of formation of NO_2 increases first followed by a rise in the rate of formation of NO and finally, a rise in the rate of formation of NDNAZ. This observation supports the conclusion that the nitroso analogue is formed by an initial cleavage of the N-NO_2 bond followed by the re-attachment of NO to the ring, as in the case of RDX and HMX. Decomposition of the TNAZ sample labeled with $^{15}NO_2$ in the nitramine group has shown that NO_2 originates from both the nitramine and the *geminal*-dinitro groups in the molecule but that the cleavage of NO_2 from the nitramine group precedes that of the C-$(NO_2)_2$ group.

Fast Heating

Laser induced decomposition of TNAZ has been studied by Garland and Nelson.[54] Through the use of time-of-flight mass spectrometry, the initial decomposition products were found. The experiment was conducted by first preparing a pellet sample of TNAZ (about 100 mg) then thermally decomposing it with a "decomposition" laser followed by an ionization pulse that was analyzed by a mass spectrometer. Selection of the decomposition pulse wavelength was made on the basis that TNAZ has a high absorption at 248 nm. A KrF eximer laser was used for the decomposition and the beam was focused normal to the sample. The resulting laser fluences ranged from 5.0 to 12.5 MW cm^{-2} (50 to 125 mJ cm^{-2}) thereby minimizing any later background ionization of TNAZ. The ionization beam was focused orthogonal to the decomposition beam and had a wavelength of 118 nm. This provided a 10.5 eV pulse that ionized most of the neutral

products. This low-energy beam was used to minimize further decomposition. Time-of-arrival scans of a number of the decomposition products were taken at various decomposition laser fluences. These scans were used to determine both the translational temperature of the products as well as to determine the temperature dependence of the relative product yields. Results of the work indicate that determination of an initial decomposition step is difficult because the relative yields for the products with high *m/z* do not change over the wide range of laser fluences. The predominant high molecular weight products found indicate three major pathways. The first fragment, mw = 176, is due to a loss of Oxygen, the second, mw = 163, a loss of NO with a later gain of H from the molecular plume, and third, mw = 146, the loss of NO_2. These pathways are also found in the decomposition of other compounds with nitroalkyl[55-57] groups.

They report that the initial steps for the thermal decomposition of TNAZ include unimolecular loss of NO and bimolecular reaction with a net loss of an oxygen atom. They found two initial decomposition channels. They are the unimolecular loss of NO and the bimolecular reaction to generate DNAZ. The unimolecular loss of NO_2 is probably an early but not initial reaction because during their Fourier transform mass spectrometry (FTMS) experiments, the high *m/z* fragments had very weak signals which indicate that TNAZ -NO_2, as well as other high *m/z* fragments may be secondary products. Through the use of FTMS, the ^{15}N labeled TNAZ (nitramine nitrogen) was studied to determine which bonds break to give the three products. The fragment corresponding to the loss of NO was found to occur by the nitramine nitro group leaving as it was the isotopically labeled. NDNAZ, loss of O, was found to occur mainly by nitroalkyl dissociation with about 20% occurring by nitramine dissociation. The loss of

an NO_2 was found in almost equal amounts, 55% nitro-alkyl and 45% nitramine. The electron impact fragmentation pathways of TNAZ were studied by Zheng *et al*.[58] Collision-induced dissociation was also used to investigate important peaks in the electron impact spectra and were used to compliment and validate the electron impact results. The major pathway in the fragmentation of TNAZ is the loss on NO_2 or HNO_2 from the dinitroalkyl group followed by the loss of an additional NO_2 or NO from the nitramine group evidenced by the isotopically labeled samples. No evidence of the loss of CH_2NNO_2 or CH_2NNO is found as is the case for RDX and HMX. This is in contrast to their previous work[44] where N-NO_2 scission was favored they find here that the C-NO_2 break first and the N-NO_2 second.

Oyumi and Brill[59] have studied thermal decomposition of some gem-dinitroalkyl cyclic nitramines including TNAZ under high rate thermolysis. Using rapid scan Fourier transform infrared spectroscopy, the gas products due to the heating at a rate between 50 and 170 K s^{-1} at various pressures of a sample of TNAZ on a filament wire have been determined. At atmospheric pressure TNAZ was heated at a rate of 145 K s^{-1} and NO_2 is the predominant initial product with the formation of a large amount of NO. Other products at this pressure include HCN, HONO, CO_2, CH_2O but no N_2O. At 30 psi, the same products are found with the exception that NO_2 is found in lesser amounts and the NO amount increases. This trend continues to a greater extent as the pressure increases. It has been concluded that NO_2 is vastly the dominant initial pyrolysis product for TNAZ. They have also reasoned that because in the thermal decomposition of RDX and HMX where the presence of H_2CO and N_2O products together indicate C-N bond cleavage and

that HCN and NO_2 products have been observed as TNAZ products but N_2O has not, TNAZ decomposes via N-N bond scission.

In a similar study two years later, Oyumi and Brill[60] have revisited the contrasting effects of pressure on the high rate thermolysis of an expanded number of energetic compounds and used rapid scan infrared spectra with a temporal resolution of 0.2 s of the first observed gas products several mm from the surface of fast heated (100 – 130 K s^{-1}) energetic materials (including TNAZ) over the pressure range of 1 – 1000 psi Ar. They have found three zones of pressure dependence for TNAZ. In the first region, below 40 psi Ar NO_2 and HONO are measured at 200 ms after reaction initiation. In the second region, 20 – 200 psi Ar, it is thought that pressure impedes the initial reaction gases and they become reagents for further reactions. In the final region above 200 psi Ar, only the least reactive gases are found i.e. CO, CO_2, H_2O and probably N_2 dominate.

Lee and coworkers[61] have used photofragment translational spectroscopy to study the decomposition mechanisms of TNAZ under different laser fluences in a molecular beam. TNAZ has been thermally decomposed via infrared multi-photon dissociation and the products were detected using quadrupole mass spectrometry. The decomposition products were dissociatively ionized by the ionization beam which complicated the results. Mechanistic information was, therefore, deduced from analysis of the time-of-arrival profiles of the fragments. At lower laser fluences, 1.4 J cm^{-2}, the initial decomposition step is proposed to be loss of NO_2 to generate DNAZ and at higher laser fluences of 10.4 J cm^{-2}, additional products were found suggesting that the DNAZ ring opens, a second NO_2 group is lost, and subsequently a N-NO_2 group is ejected. Their scheme for TNAZ is shown below.

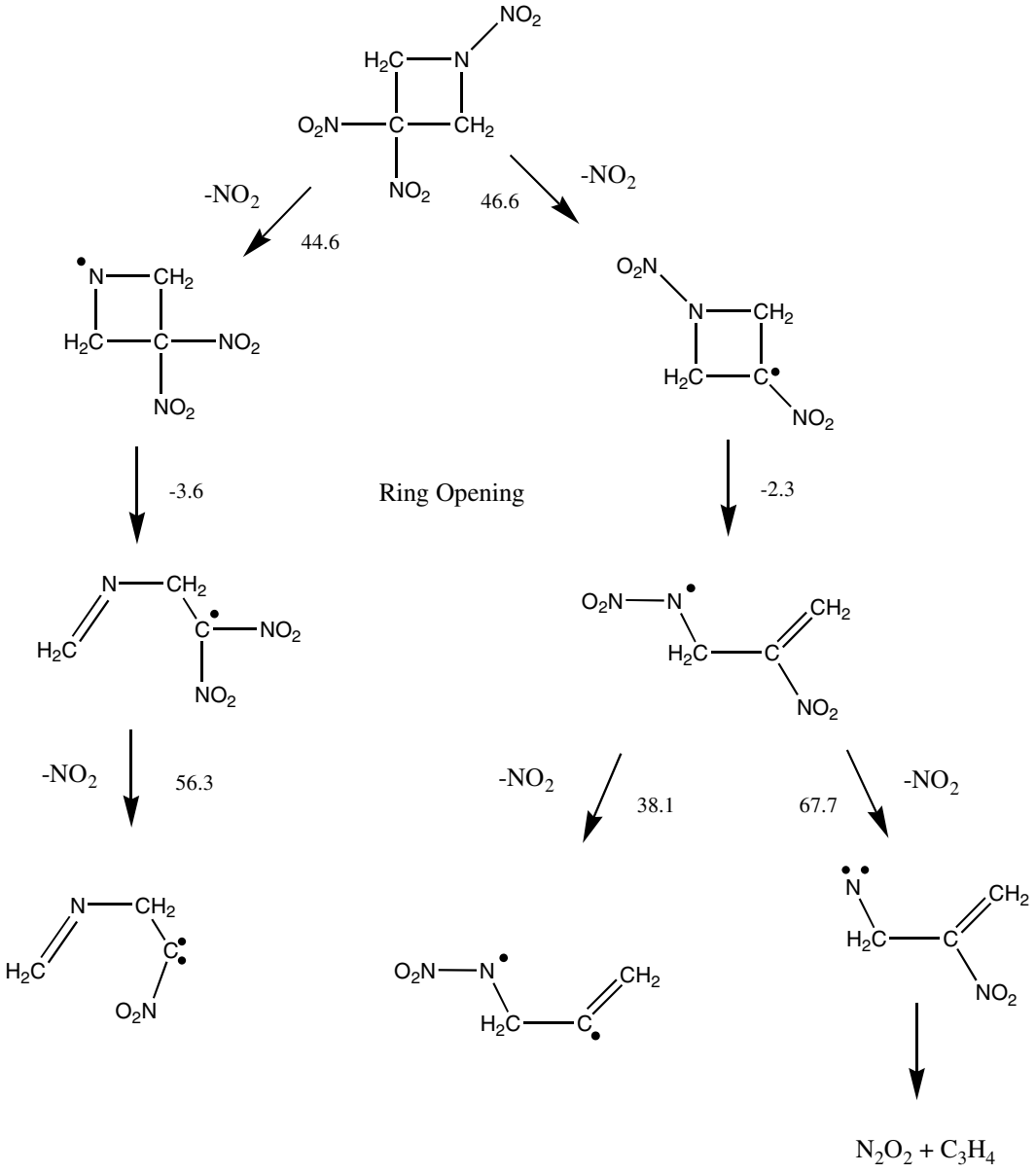

Theoretical Investigations

Wilcox, Zhang and Bauer[62] determined the heats of formation of TNAZ and its related compounds. They used a model based on the BAC-MP4 developed by Melius[63] where the lowest-energy geometry of a molecule at the 6-31G(d) level is determined followed by computing the single point MP4/6-31G(d) energy and finally adding a series

of bond length dependent energy corrections and, where appropriate, spin related corrections. The MP4 portion was replaced with the density functional method B3LYP/6-31G(d,p). The standard heat of dissociation of TNAZ by *N*-nitro and *C*-nitro bond cleavage were found to be 43.2 and 46.4 kcal/mol respectively. The reported difference between *C*-nitro in TNAZ and the higher value reported in other molecules was suggested to occur due to structural effects of the gem-dinitro moiety.

Porollo, and coworkers[64] have studied the decomposition of azetidine and its mono-, di-, and tri-nitro substituted derivatives using combinatorial enumeration based on a method called Recombination Reaction Networks. In this work every particle in a reaction is considered as a reagent. All known kinetic and thermodynamic data are used in determining the path by which the reactants find the products. They conclude that the thermal decomposition of TNAZ occurs by cleavage of both the C-nitro or N-nitro bonds as the initial step where ring fission is proposed next. They also report standard heats of formation for TNAZ (27.97 kcal/mol), 1,3-dinitroazetidine radical (44.37 kcal/mol), 3,3-dinitroazetidine radical (42.90 kcal/mol) and the nitro radical (-1.89 kcal/mol) using the semi-empirical PM3 method.[65]

Jiaoqiang and coworkers[66] found, through the use of AM1 methods, that the Wiberg bond orders of C-N bonds connecting with gem-dinitro in TNAZ and three derivatives are relatively smaller, and therefore, homolysis by breaking these bonds requires relatively low activation energies, and is probably the predominant initial reaction of thermolysis. They also found a barrier on the potential energy profile for the N-C bond break of about 50 kcal/mol using UHF-AM1 and an increment of 0.1 Å.

Zhang and Bauer[67] analyzed the thermal decomposition of gaseous nitomethane, methyl nitrite, dimethylnitramine and TNAZ using sensitivity and principle component analysis. Through the use of a much simplified mechanism the fragmentation/reaction sequence leading to final products was found. Using experimental and theoretical results of the decomposition of TNAZ and its products[68-76], a table is constructed (See Table XIII in this reference). Many of the pyrolysis reactions were found to be not significantly important in the overall reaction after the sensitivity analysis was completed. The final fragmentation/reaction sequence for the simplified scheme is given below.

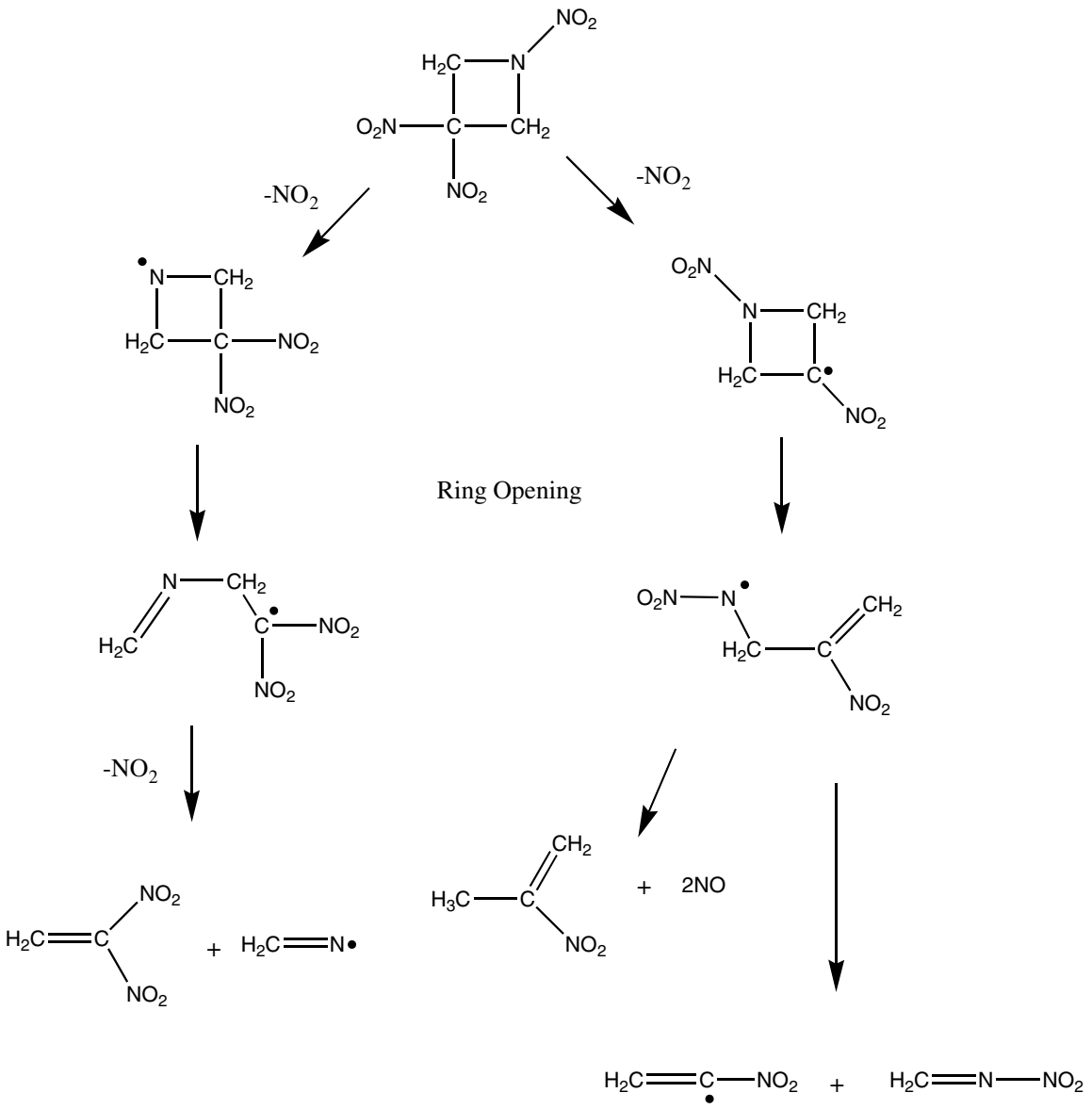

The theoretical work by Politzer and Seminario[77] show that there are three reaction pathways for TNAZ decomposition, one corresponding to each of the nitro cleavages, where the energy required to break the N-NO_2 bond is 46.6 kcal/mol and that required to break the C-NO_2 bond is 44.6 kcal/mol. They used non-local density functional theory to find the dissociation energies and report that DFT methods are quantitatively effective for calculating dissociation energies.[78-82] In their work they have

found the computed energy differed from experimental results by an average of 2.2 kcal/mol. The energies required to remove an initial NO_2 are quite similar for the two pathways (R1 and R2) which may seem surprising since C-NO_2 bonds are significantly stronger[81] than N-NO_2. Their explanation is that the 1,3-DNAZ-yl fragment is stabilized by delocalization of the unpaired electron,

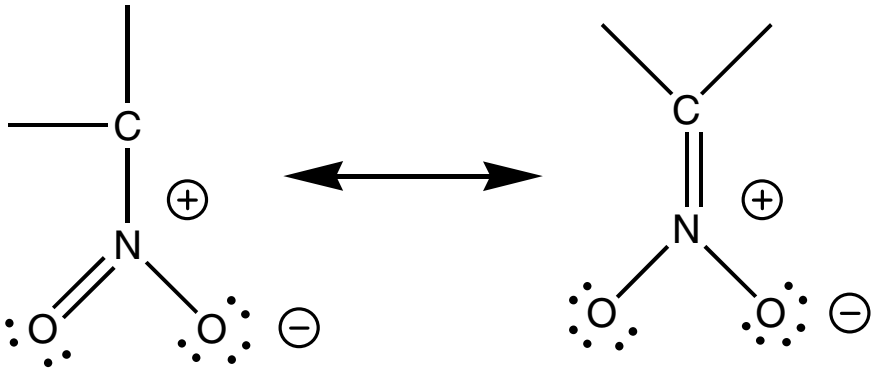

Only the part of the 1,3-DNAZ-yl fragment where the delocalization is shown.

Based on previous work[79], Politzer *et al.*[83] have found the standard gas phase heat of formation of TNAZ to be 30.7 kcal/mol based on density functional methods. The title of this work is the "Comparative computational analysis of some nitramine and difluoramine structures, dissociation energies and heats of formation". The impetus for the work was the study of lighter analogs of existing nitramines. The difluoramine structures provide higher moles of produced gas per gram ratio than that of the nitramine structure. The reported reactions for the 1-difluoramine and nitramine substituted azetidine are,

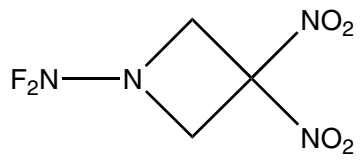

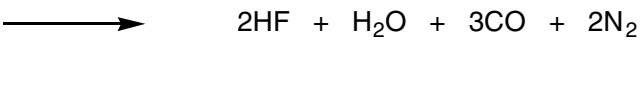

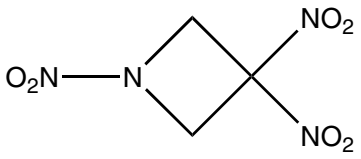

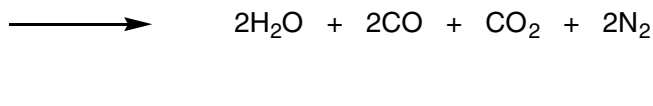

.

What seems to be in dispute here is the varying products that are produced form TNAZ. The method by which TNAZ is studied experimentally has shown that different products will form. For this case, TNAZ is of interest due to its volume of gas capacity per gram of explosive in its solid form. Only upon detonation would this quantity to some degree be measured. Unless the reported reaction is that of detonation products (the origin of the above two reactions is not given in the paper) conclusively reporting the difference of a mol gas/ g is seemingly not valid.

PART TWO

CHAPTER III

METHODOLOGY

The reactive potential energy surface (PES) used is one that models the three possible reaction paths of TNAZ unimolecular dissociation (see R1 and R2 in Chapter I). Attention was given to the reactant molecule TNAZ and the three different product fragments; TNAZ minus the alkyl NO_2 radical (subsequently referred to as 13DNAZ), TNAZ minus the nitroso NO_2 radical (subsequently referred to as 33DNAZ). Simulations were conducted using the GenDyn chemical dynamics computer code as well as certain developed subroutines written in FORTRAN92.

Equilibrium Force Field

The PES is represented by the sum of valence potential terms for TNAZ, 13DNAZ, 33DNAZ. The TNAZ force field includes three Morse terms, 14 harmonic bond-stretching terms, three harmonic wag terms, 30 harmonic angle-bending terms, and 14 truncated cosine series terms for torsional motion. The 13DNAZ fragment force field includes two Morse terms, 12 harmonic bond-stretching terms, two harmonic wag terms, 24 harmonic angle-bending terms, and four truncated cosine series terms. The 33DNAZ fragment includes two Morse terms, 12 harmonic bond-stretching terms, two harmonic

wags terms, 25 harmonic angle-bending terms, and four truncated cosine series terms. The functional forms of each term follow.

For the Morse term,

$$V_{Morse}(r) = D_e\left(1 - \exp\left[-\alpha\left(r - r^0\right)\right]\right)^2 - D_e, \quad \textbf{(20)}$$

where D_e is the bond dissociation energy, α is the range parameter and r^0 is the equilibrium bond distance. The bond dissociations computed by Politzer and Seminario were used for D_e values for N-NO_2 and C-NO_2.[77] The harmonic type terms, bond-stretching, wag, and angle-bending have the harmonic oscillator functional form,

$$V_{harmonic}(q) = \frac{1}{2}k\left(q - q^0\right)^2, \quad \textbf{(21)}$$

where the internal coordinate q takes the value of r for bond-stretching, γ for wags and θ for angle-stretching and k represents the appropriate harmonic force constant. The q^0 corresponds to the respective equilibrium internal coordinate. The torsional terms are given by the truncated cosine series,

$$V_{torsion}(\tau) = \sum_{i=0}^{4} a_i \cos(i\tau), \quad \textbf{(22)}$$

where τ is the torsional (dihedral) angle and a_i are the Fourier coefficients that conform the function to the desired curvature. The values of the potential parameters are given in Tables XIV – XVI.

The reactive PES for TNAZ is a collection of equilibrium force fields for the reactant molecule TNAZ and each of the three fragments and the mathematical path between them given by switching functions. The TNAZ force field was fit to both experimental and *ab initio* data. Normal mode frequencies were fit to the experimental vibrational frequencies of Yu *et al.*[43] and scaled *ab initio* calculations. Normal mode

displacements (eigenvectors) are based on *ab initio* calculations. All three product fragments are radicals and therefore no useful experimental data are available. The products are fit solely to *ab initio* calculation data.

Potential Energy Surface Fitting

The reactant TNAZ and products 13DNAZ and 33DNAZ equilibrium force fields were fit to normal mode frequencies and eigenvectors. All potential force constants were considered variables in the minimization. As a starting point, only bond stretching force constants were considered that were intuitively assigned based on bond strengths. An iterative least squares fit of the data set was conducted until the root mean square deviation was minimized. Bond angle force constants were then added as parameters, then wagging angle force constants and finally torsional terms. An informal routine was developed where priority was assigned to the frequency or eigenvector with the largest root-mean-square error. This method enables a starting point for the minimization and as a datum falls within an acceptable error it is 'locked' and no longer varied during the minimization. At certain times the minimization would find local minima that were well above an acceptable error. The minimization routine would recognize this and apply a random perturbation to the current data set to move the routine along.

Ab Initio Calculations

In a previous paper[84] it was shown that the use of density functional theory is a reasonable alternative to the more demanding MP2 calculations when the geometrical structures, harmonic vibrations, and the relative stability of various tautomers are of interest. The DFT calculations were done using B3LYP exchange-correlation functionals which uses the exchange functional described by the fitted three-parameter

hybrid of Becke[85] and the gradient corrected correlation energy functional of Lee, Yang and Parr[42]. The 6-31G(d,p), (spilt-valence plus d-type and p-type polarization functions) basis set was used. The frequencies were scaled[86] by 0.9613 to correct for the over estimation of vibrational frequencies. As a check for the validity of the reported scaling of *ab initio* frequencies, the known experimental frequencies were each compared to corresponding non-scaled *ab initio* frequencies. See Table XIX. The reported scaling of 0.9613 compared well with the average scaling as described above of 0.9777. Although the difference is less than two percent, the more important feature to note is that the scaling is not uniform. Notice that there is better correspondence between the lower frequencies than that of the higher ones. A possible explanation of this behavior may lie in the approximations inherent in the density functional theory. Higher frequencies are dominated by one type of integral and the lower frequencies are dominated by more than one integral. Density functional theory uses a function that describes the electron density around each nuclei.

Switching Functions

In an effort to model the unimolecular decomposition of TNAZ in a somewhat chemically intuitive way, the reactant molecule is "connected" to the products by a smooth path via mathematical switching functions. Some of the early work that involves switching functions was done by Bunker and coworkers[87-90] who used the switching function formalism to derive an analytic potential energy surface for the reaction, $O + OH \leftrightarrow HO_2 \leftrightarrow O_2 + H$, and subsequently used it in trajectory calculations for highly excited HO_2. Varandas[91,92] has used switching functions to connect two potential forms of a bound system. The two potential terms correspond to the form that acurately

approximates the available spectroscopic data (which is accurate in the vicinity of the potential well) and the potential form that accurately approximates the potential well depth at the equilibrium geometry (which is accurate in regions away from the potential minimum). Budenholzer[93] modified an exsisting four-body polynomial function potential[94] with switching functions to ensure the proper asymptotic state of the reaction products and to avoid unphysical areas in the potential energy function for the unimolecular dissociation of HFCO. The use of switching functions in reaction dynamics is common and the above examples should not be taken as comprehensive. To be sure, there have been many studies of reaction dynamics in which switching functions have been employed[95-98].

In the present work, reactant parameters are switched to product parameters with the function,

$$S(r_i) = 1 + a\tanh[b(r_i - r_i^0)^n] \qquad (r_i > r_i^0)$$

$$S(r_i) = 1 \qquad \text{(otherwise)} \qquad \textbf{(23)}$$

where r_i represents the C-NO_2 and N-NO_2 bonds in TNAZ. The b and n parameters control the position and rate of switching. Figure 6 shows an arbitrary switching function that has been superimposed upon the Morse potential term of the N-N bond of TNAZ to show that the switching parameter b and n have been chosen to model the dissociation of TNAZ. The switching parameters for the TNAZ dissociation were chosen as b = 0.2 and n = 3. The switching parameter a in Equation 23 is a constant for each switched coordinate within each reaction channel. It is defined by,

$$a = \left[\frac{Q^p}{Q^r}\right] - 1, \qquad \textbf{(24)}$$

where Q represents a particular coordinate (geometrical parameter or force constant). The superscript p denotes the product state coordinate and the superscript r denotes the reactant state coordinate. The switching of force field parameters is then accommplished using,

$$Q = Q^r S(r_1) S(r_2) S(r_3) . \quad \textbf{(25)}$$

As the molecule dissociates, one of the r_i's in Equation 25 becomes large, thereby diminishing the contribution of the other two switching functions. One can imagine the competition that takes place as each reacting bond "pulls" towards its respective product.

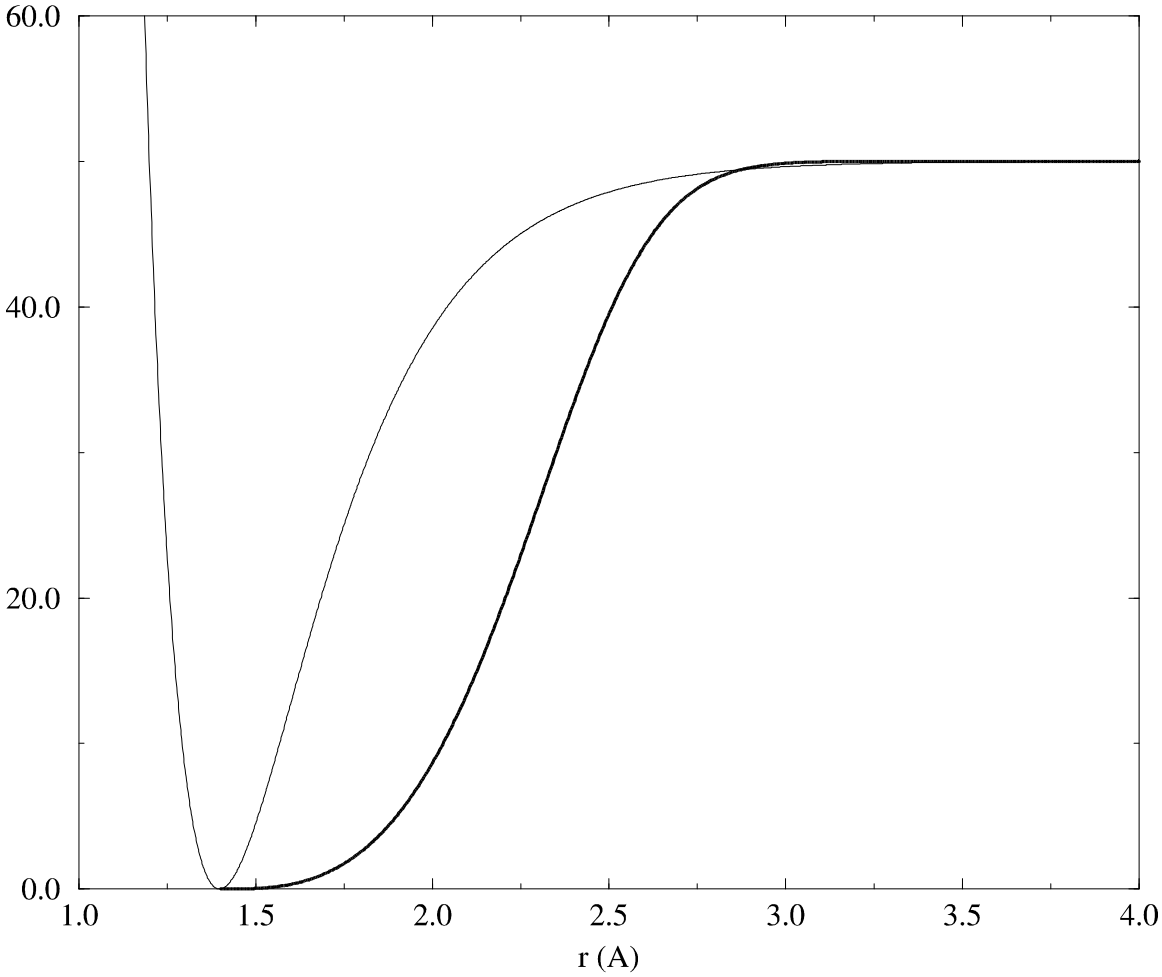

Figure 6. The dark curve represents the switching function that attenuates an arbitrary parameter that has the value of zero for reactants and 50 for products. The light line represents the Morse curve of the N-N bond in TNAZ. The two curves are superimposed to show the proper choice of parameters of the switching function, i.e. as the reactant moves to products the attenuation should follow the progression of the reaction in such a way as not to attenuate too early but attenuate completely before the bond breaks.

Starting with the TNAZ reactant molecule, each coordinate is attenuated to the appropriate product coordinate by one of the three possible bond scissions. To facilitate an understanding of the PES, the following example is given. As the N–N bond vibrates past its equilibrium posititon, the molecule tends towards the two product fragments TNAZ(N–NO_2) and NO_2. The force constants and geometric parameters of the reactant molecule TNAZ are smoothly connected to those of the product fragments by using

Equation 23 in the potential terms. Consider the harmonic bond-stretching term of the C-C bond which has the potential term (with switching),

$$V_{C-C}(r_{C-C}, r_1, r_2, r_3) = \frac{1}{2}\prod_{i=1}^{3} S(r_i) k_{C-C}\left(r_{C-C} - \prod_{i=1}^{3} S'(r_i) r_{C-C}^{0} \right)^2 . \quad \textbf{(26)}$$

The C-C bond potential is a function not only of its bond length, $r_{C\text{-}C}$, but also on each of the three reaction coordinates, which in this case are the three nitro-bonds noted as r_1, r_2, and r_3. Notice also the prime on the equilibrium bond length switching function which indicates that it is distinctly different from that of the switching function of the force constant

Trajectory Calculations

The efficient microcanonical sampling (EMS) procedure[99] consists of a random walk through the configuration space of the reactant followed by selection of the atomic momenta so as to ensure a microcanonical ensemble of trajectories. The Markov chain is generated in the reactant configuration space using a weight function of the form[100],

$$W(E,0) = \frac{\left[E - V(q)\right]^{(3N-8)/2}}{\sqrt{\left(I_A I_B I_C\right)^{-1}}}, \quad \textbf{(27)}$$

where E is the desired energy of the microcanonical ensemble, $V(q)$ is the potential energy associated with some configuration q. N is the number of atoms in the molecule, and I_A, I_B and I_C are the eigenvalues of the moment of inertia tensor[101]. Momenta were selected so that there was no center of mass motion and the molecule contained no net angular momentum.

Starting from a configuration $\mathbf{q}_k$, one or more of the position coordinates are moved to yield a trial configuration $\mathbf{q}_{k+1}$. The trial configuration $\mathbf{q}_{k+1}$ is accepted or rejected based on the following criteria: The random walk is restricted to configurations

corresponding to the reactant molecule. If the trial configuration $\mathbf{q}_{k+1}$ results in a configuration that is inconsistent with this restriction, then the trial configuration $\mathbf{q}_{k+1}$ is rejected and the configuration for state k+1 is taken to be the same as for state k. Otherwise, if the statistical weight (see Equation 27) for trial configuration $\mathbf{q}_{k+1}$ is greater than that of configuration k then the trial configuration is accepted as state k+1. Otherwise, the ratio W_{trial}/W_k is compared with a random number between 0 and 1. If the ratio is larger than the random number then the trial configuration $\mathbf{q}_{k+1}$ is accepted as state k+1. Otherwise, trial configuration $\mathbf{q}_{k+1}$ is rejected and the configuration for the state k+1 is taken to be the same as that for state k.

Microcanonical ensembles of 1000 trajectories were computed at ten different energies ranging from 250 – 700 kcal/mol at increments of 50 kcal/mol. Trajectories of 200 kcal/mol were computed at 100 ps but there were not enough dissociations to warrant a valid run. Computations over 100 ps of simulation time were not feasible. Non-statistical behavior was observed at energies above 800 kcal/mol. The random walk was initiated by placing TNAZ in its equilibrium greometry after which a warm up walk of 1,000,000 steps was performed to move the molecule away from the initial configuration. All 17 atoms were moved at each step of the chain. The maximum allowable step size for each atom was chosen such that an acceptance probability of between 0.45 and 0.55 was achieved at each energy. Maximum extentions of individual bonds were imposed in order to restrict the Markov chain to reactant configurations. The length of the initial walk was chosen to ensure convergence of average values, such as potential energy and internal coordinates. Values of the momenta were then selected to ensure a microcanonical ensemble and the trajectory was computed. After the first trajectory, the

original Markov chain was continued, with every $100{,}000^{th}$ subsequent configuration being used as the initial geometry for a trajectory. Each trajectory and its outcome (i.e. dissociation, reaction time etc.) were counted *m* times, where *m* is the number of times the initial configuration of the trajectory was repeated in the Markov chain. This procedure was repeated until the desired number of trajectories was computed.

Trajectories were integrated in a lab-fixed Cartesian coordinate system, using a fourth-order Runge-Kutta-Gill routine with a fixed step size of 1×10^{-16} s and 1×10^{-17} s depending on the length of simulation time needed to attain a significant number of dissociations.

PART TWO

CHAPTER IV

RESULTS AND DISCUSSION

The unimolecular dissociation of TNAZ has been studied using classical trajectory methods. Ensembles of 1000 trajectories at a range of energies have been used to determine power spectra, the overall rate of dissociation, rate of individual reaction channels, and branching ratios. The results and discussion are covered as follows: Vibrational frequencies are presented, compared and discussed; Equilibrium and switching potential energy surface spectra are presented; A representative trajectory is shown to illustrate energy conservation and dissociation; computed rates and experimental rates comparison criteria are given; computed rates and branching ratios are presented compared and discussed; comments on Rice-Ramsberger-Kessel behavior are presented.

Vibrational frequencies were computed for TNAZ, 13DNAZ, and 33DNAZ and are given in Tables XVII and XVIII. The highest 31 frequencies are in excellent agreement with their target frequencies. Unlike the higher frequencies that represent bond stretching and angle bending the lower frequencies represent molecular motions that are more complex in comparison. The chosen potential parameters lend well to accurately computing their frequencies. The challenge is then to represent the lower

more complex normal mode motions of the molecule in terms of only bond stretching, angle bending, wagging and torsional potential functions. The consequences are somewhat lessened in that these low frequencies contribute to a less extent to the reaction coordinate. This has been shown preliminarily in intra-molecular vibrational energy re-distribution (IVR) [102] studies.

Power-spectra were computed to confirm that the trajectories are not deviating significantly from normal mode analyses. Ten trajectories were run for 16.678 ps with a time step of 0.1ps. The internal coordinates of the molecule were averaged over the ten trajectories and stored as a function of time where the spectral density was subsequently found. The resolution of the spectral plots is 2 cm^{-1}. There were no negative frequencies observed. Figures 8 and 9 show the auto-spectral density function of the equilibrium force field for TNAZ and switched potential energy surface respectively. A difference spectrum between the equilibrium potential energy surface and the switched potential energy surface was also computed as shown in Figure 7. There is good agreement between the positions of spectral peaks and calculated frequencies from normal mode analyses.

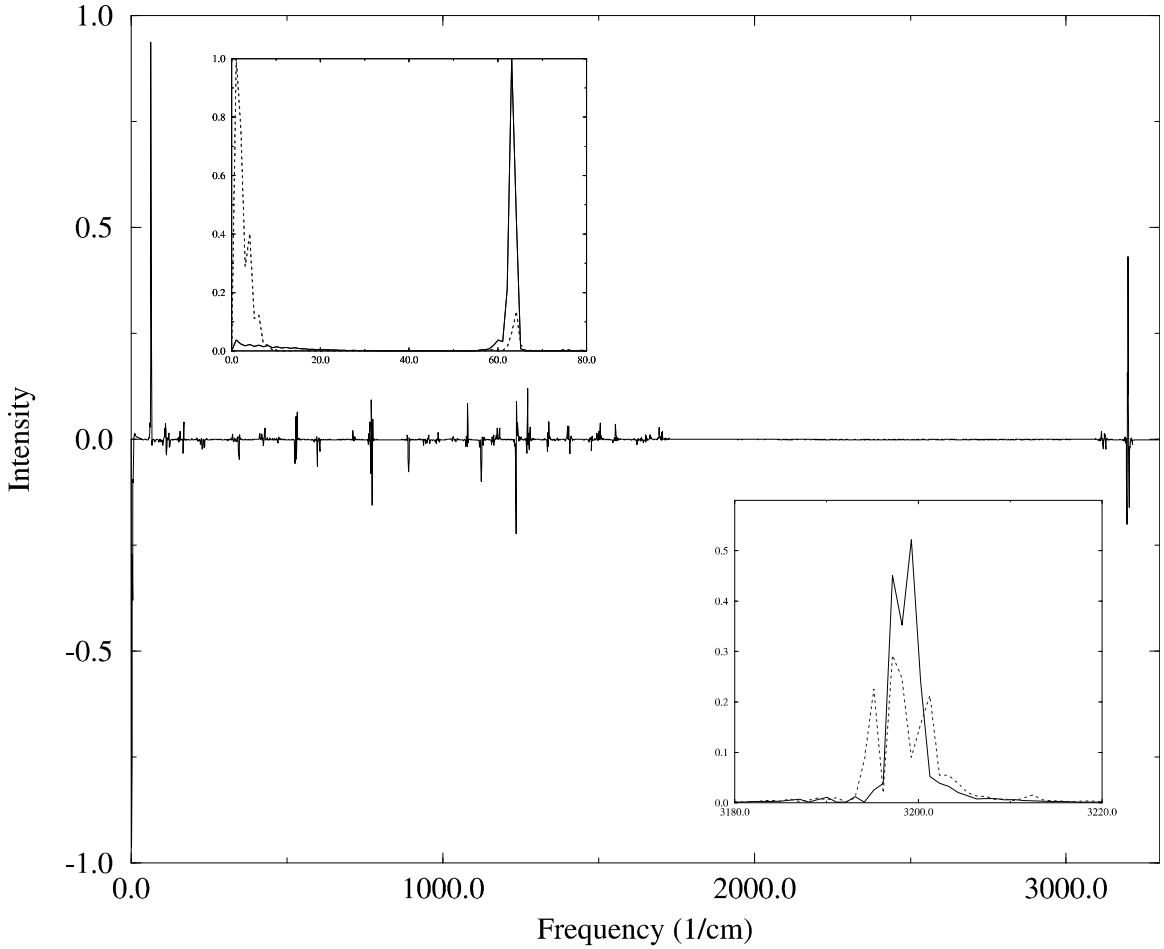

Figure 7. Difference spectrum between the auto-spectral density function of the equilibrium force field and that of the switched potential energy surface. The two insets are superpositions of the auto-spectral density functions to show the correspondence of the two. The equilibrium force field spectra is represented by the solid line and the switched PES spectra is represented by the dashed line in the insets. Notice that there is a general correspondence between the frequencies and that the differences occur between the intensities.

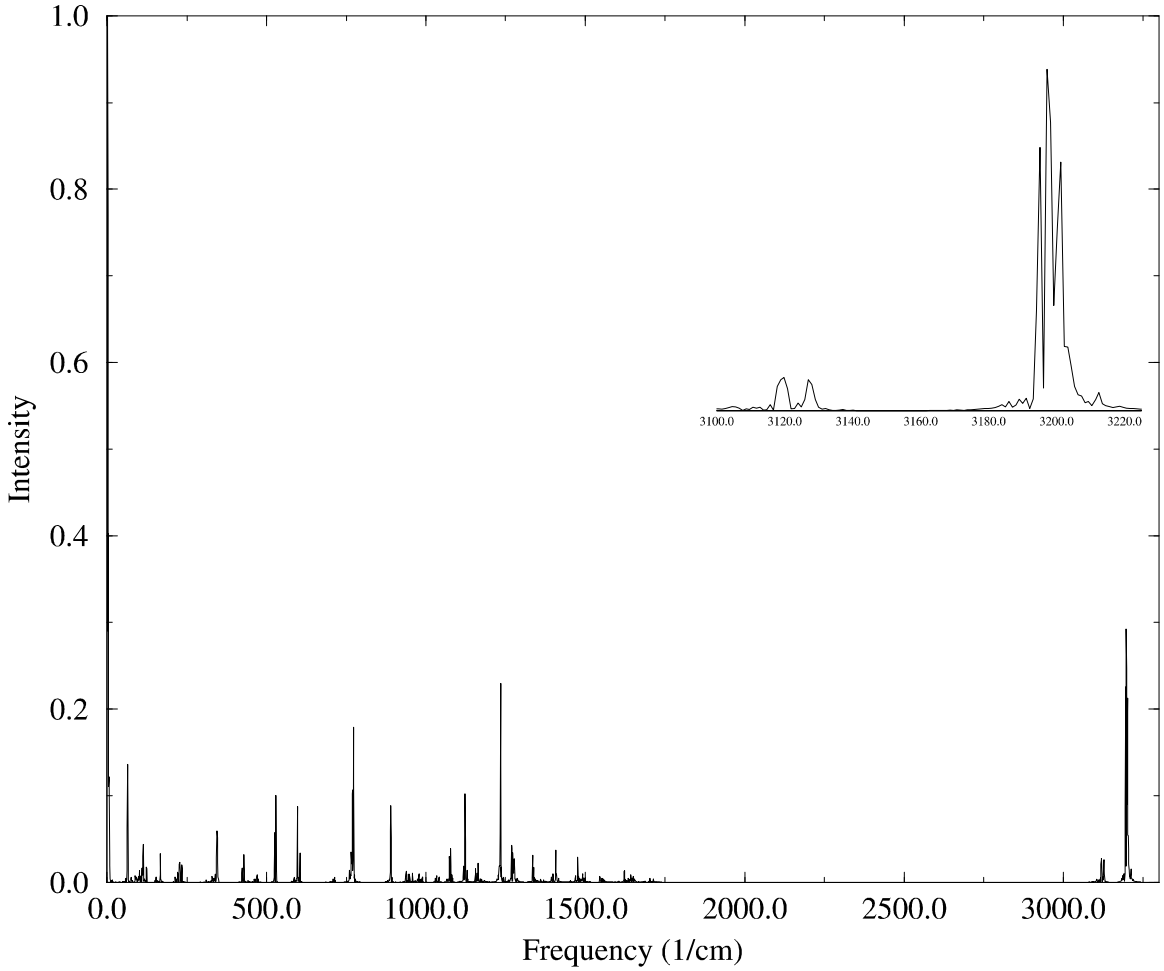

Figure 8. The auto-spectral density function of the switched PES for TNAZ. Ten trajectories were run for 16.678 ps with a time step of 0.1 ps. The internal coordinates of the molecule were averaged over the ten trajectories and stored as a function of time where the spectral density was subsequently found. The resolution of the spectral plot is 2 cm^{-1}. The inset shows the fine structure of the highest frequencies.

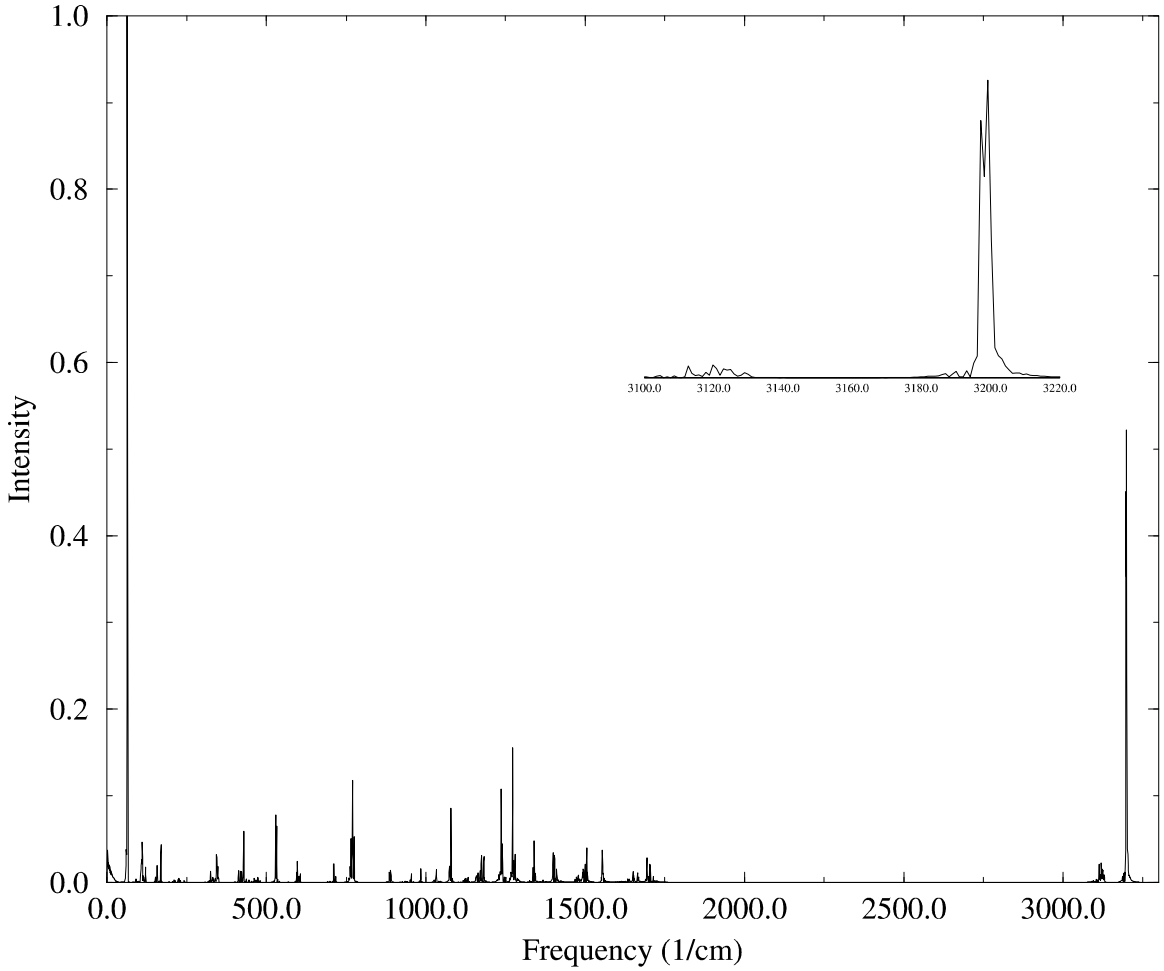

Figure 9. The auto-spectral density function of the equilibrium force field for TNAZ. Ten trajectories were run for 16.678 ps with a time step of 0.1 ps. The internal coordinates of the molecule were averaged over the ten trajectories and stored as a function of time where the spectral density was subsequently found. The resolution of the spectral plot is 2 cm^{-1}. The inset shows the fine structure of the highest frequencies.

To further validate the reactive potential energy surface, a representative trajectory where dissociation occurs is shown in Figure 10. Here, the N-NO_2 bond is broken at approximately 0.35 ps. Batches of test trajectories were used to ensure that the choice of 3.0Å as the 'bond-broken' criterion does neither hinder the dissociation nor add erroneous dissociations.

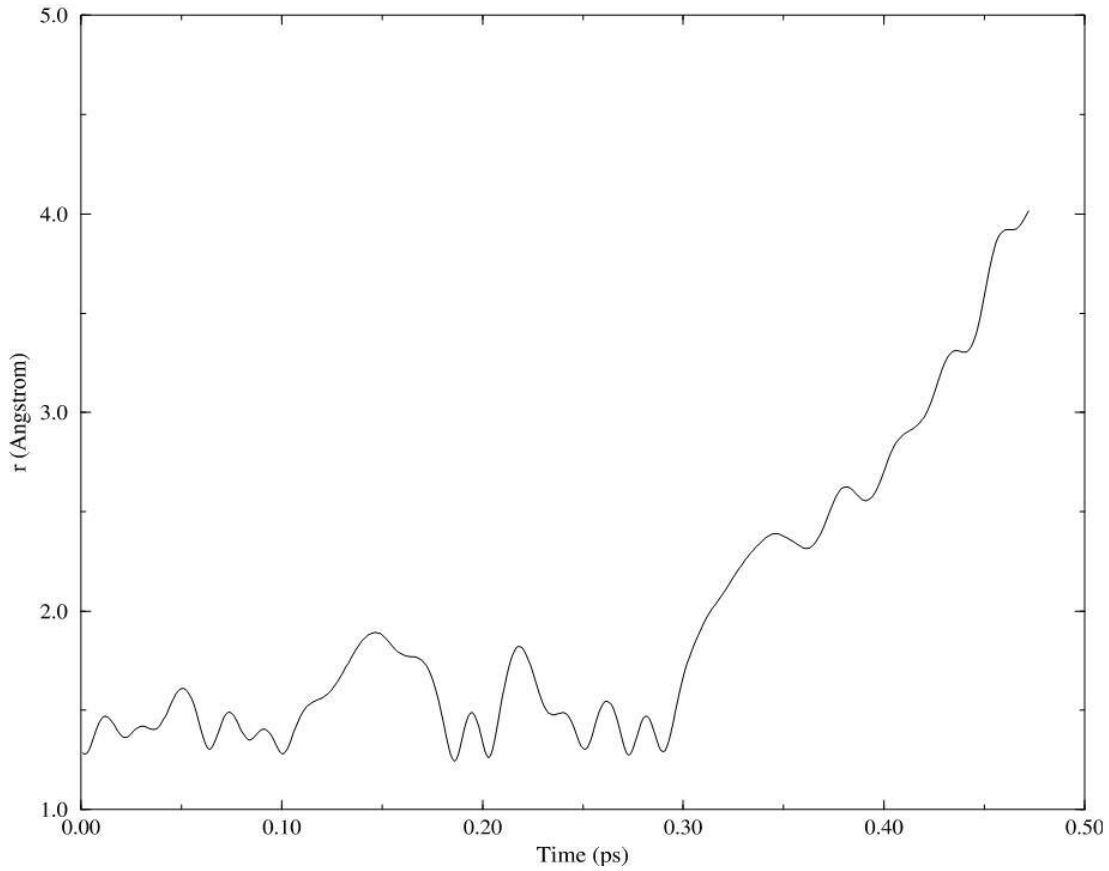

Figure 10. A representative trajectory using the switched potential in which dissociation occurs. In this case the N-N bond is monitored as a function of time and the bond was "broken" after the N-N bond distance became larger than 4 Å. The total energy for this trajectory was 400 kcal/mol.

Additionally, the conservation of energy was monitored for the lowest energy considered of 250 kcal/mol, representing on an average, 5.56 kcal/mol per vibrational degree of freedom. At this low energy, very few trajectories are reactive ones as the lifetime for this energy range is about 76 ps. As the integration step size is increased, the total system energy will not conserve as well as that of a smaller step size. The integration step size is, therefore, chosen to minimize the simulation trajectory time while maintaining the conservation of energy. Figure 11 shows a typical trajectory run using the switched potential for TNAZ at 200 kcal/mol. The trajectory was run for 100 ps with

a step size of 0.01 fs. The simulation time needed for these, long trajectory, small step size runs was on the order of 200 hours using an IBM RISK 6000 AIX 4.3.2 operating system and a modified GenDyn[103] computer code written in FORTRAN92. As stated earlier, the total energy in the molecule is 250 kcal/mol where the potential minimum is -137.8 kcal/mol (sum of the Morse term potential well depths). At the termination of the trajectory, the energy has been conserved to within 99.7%.

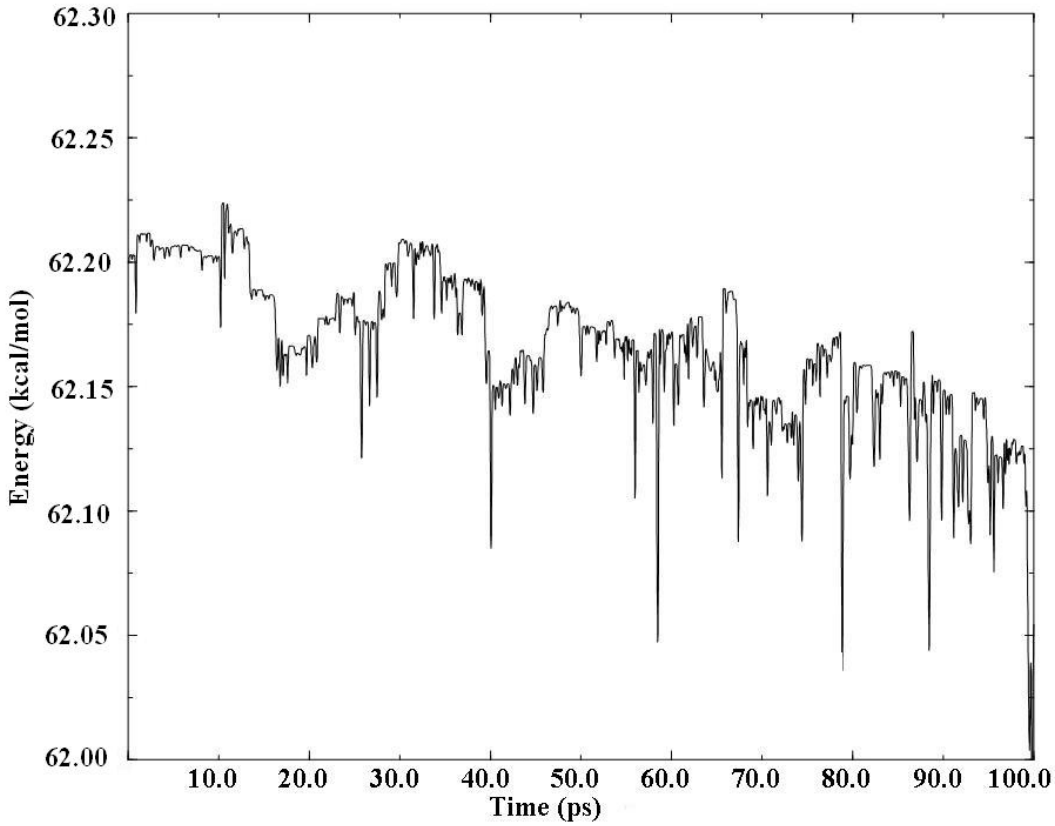

Figure 11. A typical trajectory run using the switched potential for TNAZ showing the temporal conservation of energy. The trajectory was run for 100 ps with a step size of 0.01 fs. The total energy in the molecule is 200 kcal/mol where the potential minimum is at -137.8 kcal/mol. At the end of the trajectory the energy has been conserved to 99.7%.

As a particular trajectory is computed, the number of reactive trajectories is counted along with the identity of the bond that has dissociated. The first order decay plots are presented in Figure 12 with ten panels corresponding to the ten total energies.

The number of unreacted trajectories at time t, (N_t), divided by the total number of trajectories in the ensemble, (N_0) is plotted vs. time in picoseconds. The first order rate coefficients for the overall reaction process were then computed by fitting the lifetimes to,

$$\ln\left(\frac{N_t}{N_0}\right) = -kt\,, \qquad \textbf{(28)}$$

where k is the first order rate coefficient. Trajectories run at 600 kcal/mol and higher have a non-linear region early on, indicative of IVR. A characteristic of trajectories at energies above 300 kcal/mol is the later-time non-statistical behavior. At later times in these trajectories most all molecules have dissociated. Those that do in this region are few and are therefore do not represent a statistical sample.

Table XX shows the calculated rate, experimental rate, extrapolated temperature, and percent error for each of the ten energies considered. The computed rates are within extrapolated experimental results error.

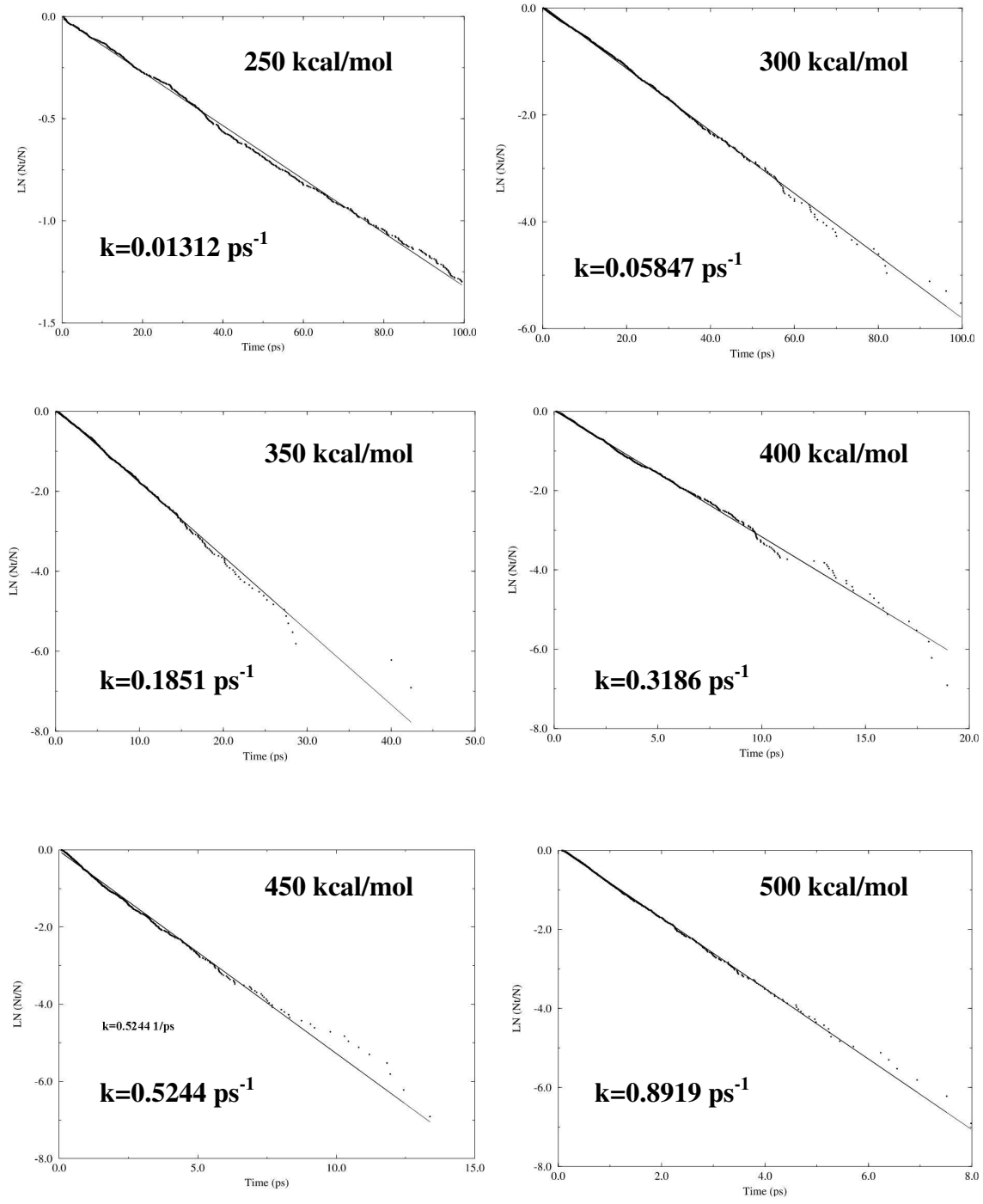

Figure 12. Plots of first order decay curve for the unimolecular dissociation of TNAZ. The first order rate coefficient *k* for a microcanonical ensemble of 1000 trajectories at a range of 250 - 700 kcal/mol at 50 kcal/mol increments was obtained by the least-squares fit to Equation 28. Panels are distiguished by their energies.

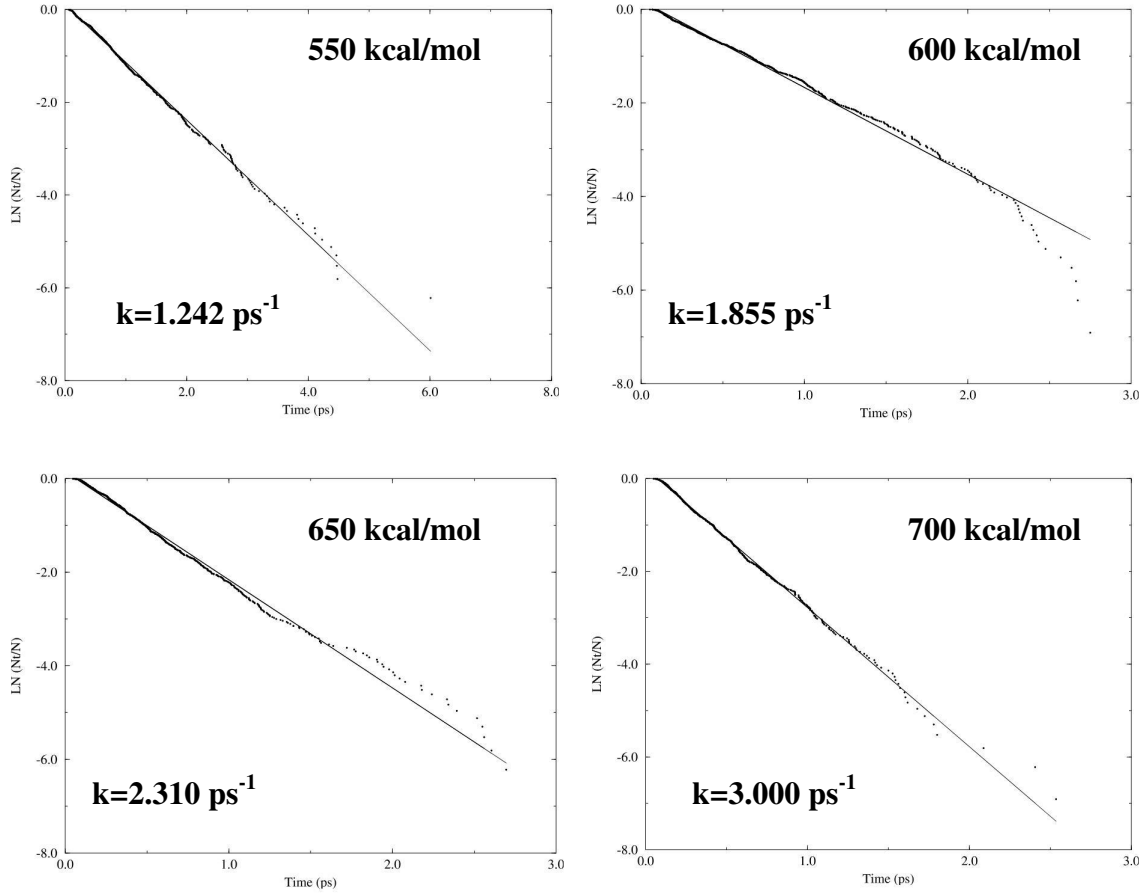

Figure 12. Continued. See page text for comments.

The overall reaction rate coefficient k may be expressed in terms of the three rate coefficients for each reaction channel,

$$k = k_{NN} + k_{CN} + k_{CN'}, \quad \textbf{(29)}$$

where k_{NN} is the rate coefficient for the dissociation of the N-NO_2 bond, k_{CN} is the rate coefficient for the dissociation of the axial C-NO_2 bond, and $k_{CN'}$ is the rate coefficient for the dissociation of the equatorial C-NO_2 bond. Reaction rate branching ratios were determined for N-NO_2:C-NO_2 dissociations and C-NO_2(axial):C-NO_2(equatorial) dissociations. These are shown as raw data in Table XXI and plotted with linear trend lines in Figures 13 and 14.

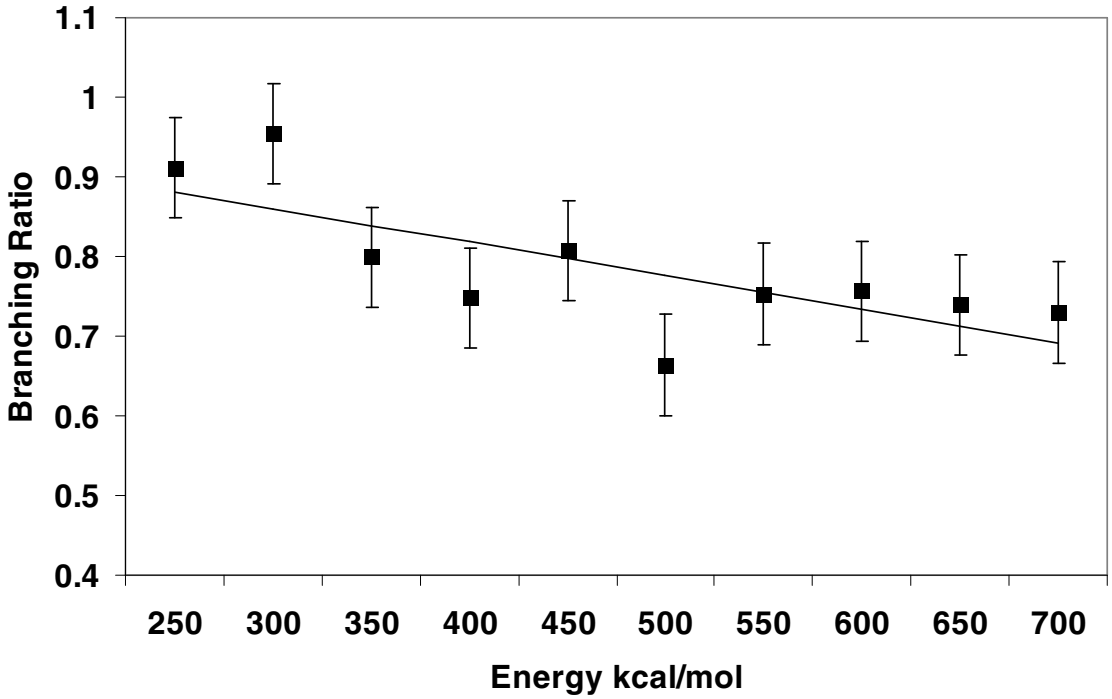

Figure 13. Branching ratios of N-NO_2 to C-NO_2 scissions at the ten energies.

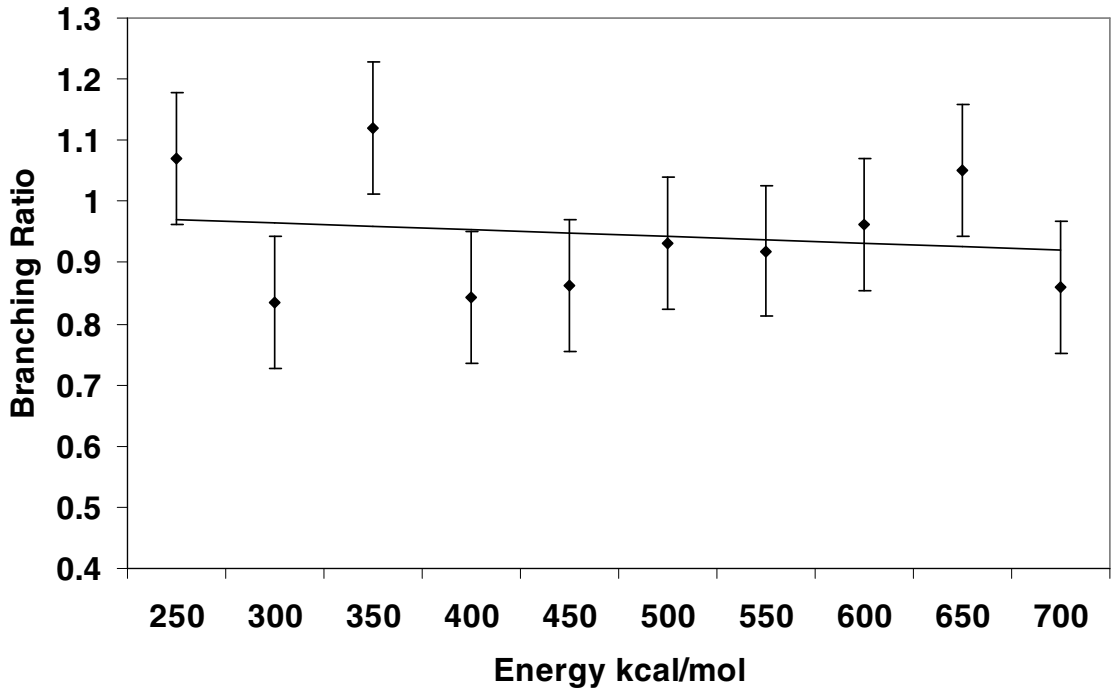

Figure 14. Branching ratios of the C-NO_2 scissions at the ten energies.

The experimental rates determined by Zhang and Bauer[33] occurred over the temperature range of 750 – 1100 K in the high pressure limit. The microcanonical molecular dynamics simulations of the current work were computed over the energy range 250 – 700 kcal/mol. The calculations were for ensembles of trajectories where all energy was deposited as vibrational energy. The relationship between energy and temperature is given in terms of $k_B T$, and the vibrational partition function by,

$$E = (3n-6)k_B T\,, \tag{30}$$

and,

$$E_{vib} = Nk_B \sum_{j=1}^{\alpha}\left(\frac{\Theta_{vj}}{2} + \frac{\Theta_{vj}\exp\left(-\Theta_{vj}/T\right)}{1-\exp\left(-\Theta_{vj}/T\right)}\right), \tag{31}$$

respectively, where $\Theta_{vj} = h\nu_j/k_B$, $\alpha = 3n\text{-}6$, ν_j is the vibrational frequency, h is Plank's constant k_B is Boltzman's constant N represents the number of molecules and n is the

number of atoms which in this case is one and 17, respectively. Figure 15 shows the relationship between energy and temperature over the range concerned.

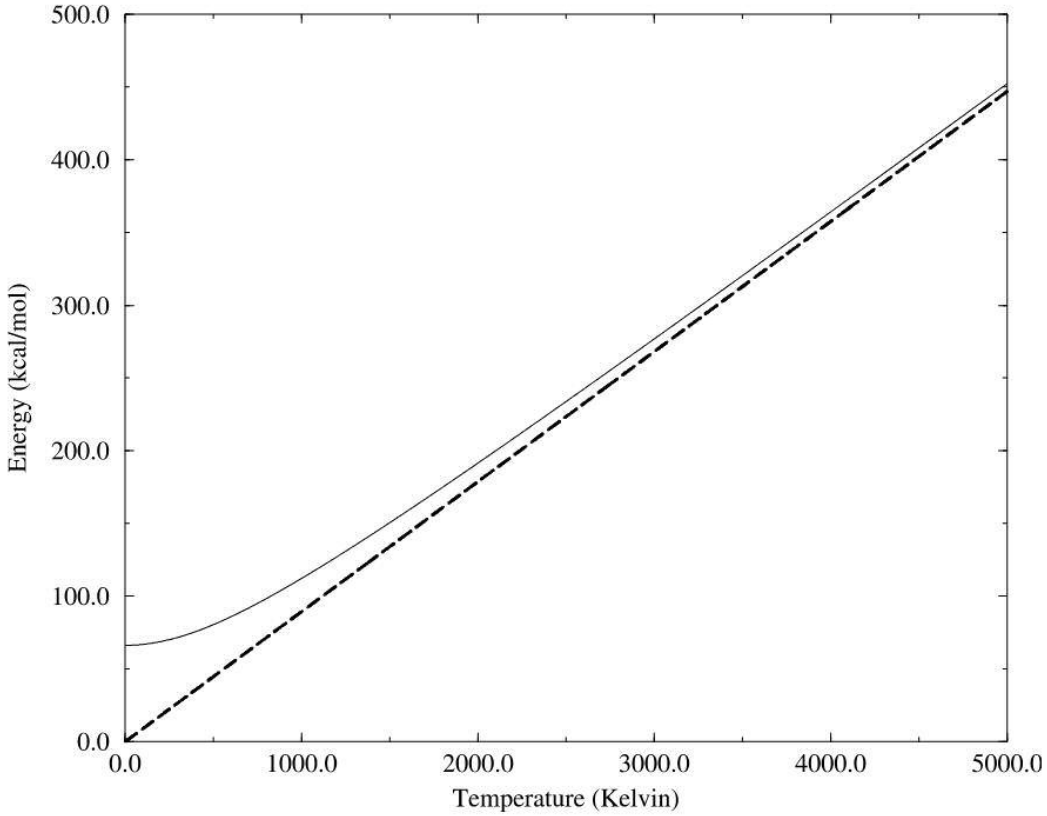

.

Figure 15. Relationship between energy and temperature in terms of *k*T and the vibrational partition function (Eq. 30 and 31). The solid line shows the correspondence between the microcanonical ensemble energy and experimental temperatures by using the vibrational partition function. The dashed line is found by Eq. 30.

The comparison between theoretical and experimental work is given in Figures 16 and 17. The extrapolated experimental data with error are plotted along with both energy-temperature comparison scenarios (Equations 30 and 31). Figure 16 is the comparison between computed rates and extrapolated experimental data. Figure 17 is the comparison between experimental rates and extrapolated computed rates. The extrapolated computed rate constants extend below the lower experimental error as temperature decreases.

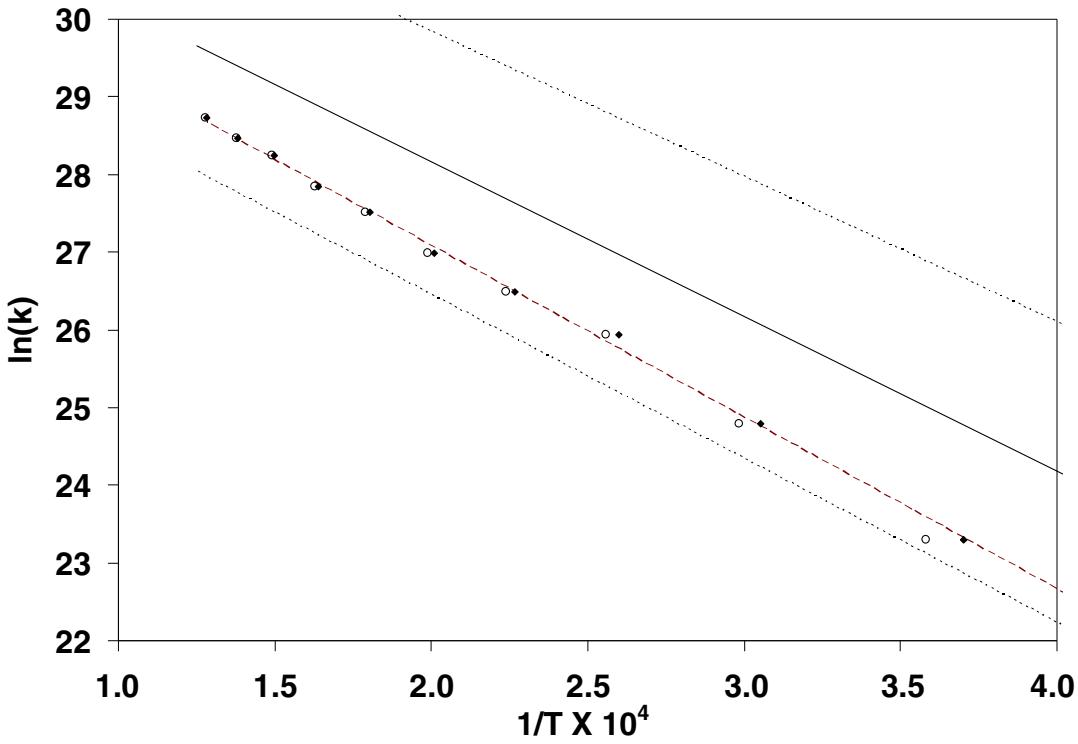

Figure 16. Comparison between computed rates and extrapolated experimental work. The solid line and parallel short dashed lines represent the experimental data with error (short dashed lines). The computed rates are plotted as filled diamonds where T is found from Equation 31. The empty circles represent the rates using $(3n\text{-}6)k_BT$. The long dashed line is the linear fit to the black diamond data.

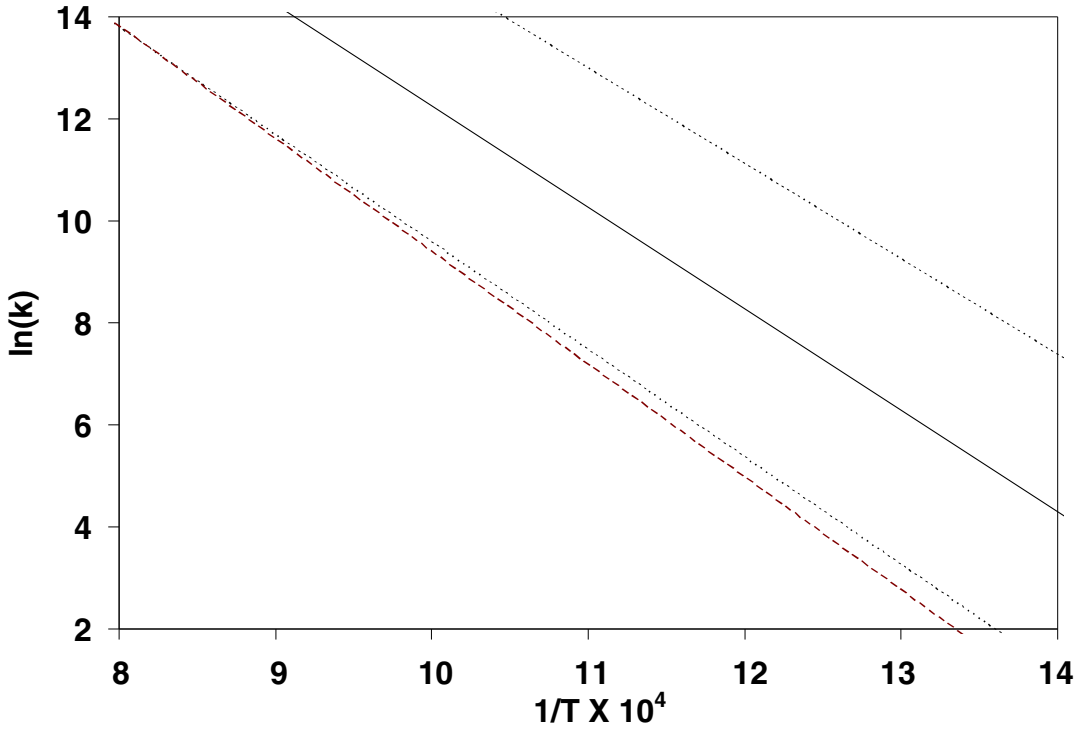

Figure 17. Comparison between extrapolated computed linear regression (shown as long dashed line) and experimental region of the rate of dissociation of TNAZ. At 700K the computed rate is 0.9523 s^{-1} and the lower limit error experimental rate is 1.753 s^{-1}. At 1100K the computed rate is 9.224×10^4 s^{-1} and the lower limit error experimental rate is 1.004×10^5 s^{-1}.

Rice-Ramsperger-Kassel (RRK) theory predicts the unimolecular dissociation of a gas as a function of the energy it contains and is proportional to its internal degrees of freedom. In the high pressure limit, where the rate of intramolecular energy redistribution is rapid compared to the rate of reaction, the RRK theory may be applicable. This is given by the RRK equation,

$$k(E) = A\left(1 - \frac{E_0}{E}\right)^{s-1}, \qquad \textbf{(31)}$$

where A is the frequency of the s contributing classical oscillators and E_0 is the energy required to energize the critical mode leading to, in this case, a dissociation. Figure 18 is the RRK plot of the computed first order rate coefficients for the dissociation of TNAZ.

The linear least square fit yields s = 47.9 and A = 43.5 ps^{-1} (4.35×10^{13} s^{-1}).

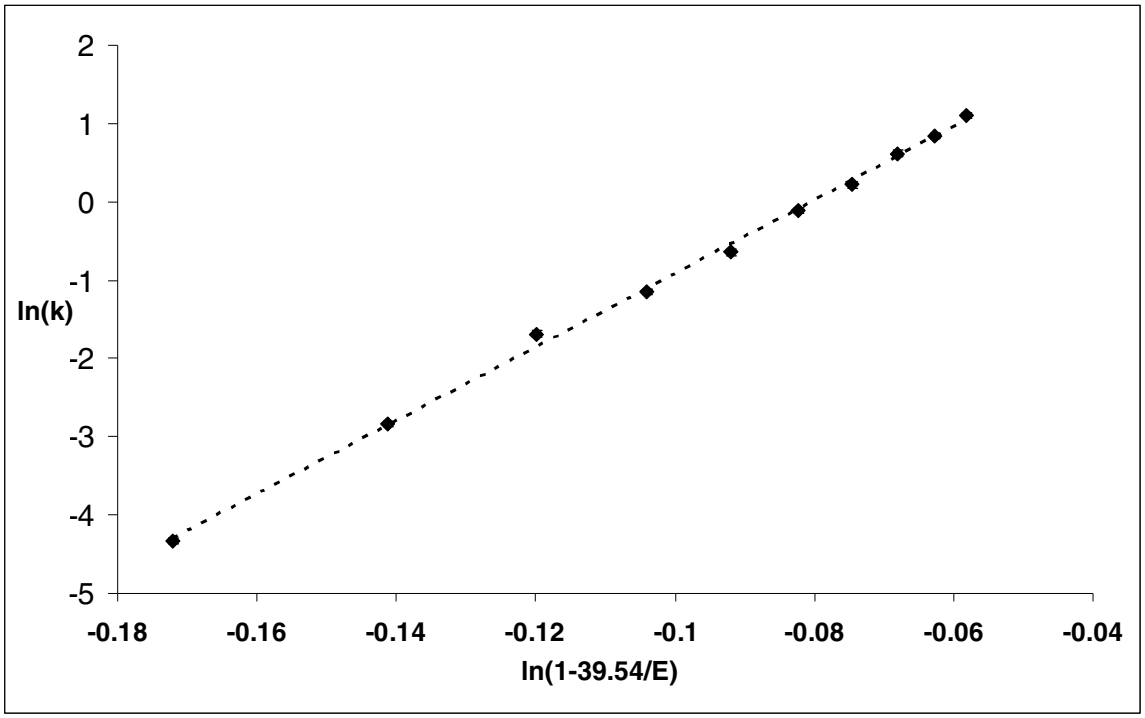

Figure 18. Simulations computed rate constants (k), are plotted according to Equation 31 where, 39.54 kcal/mol is the activation energy for dissociation, to show the correspondence to RRK and are represented by the black diamonds. The linear fit to these data is shown by the dashed line where s=47.9 and A=43.5 ps^{-1}.

Table VII. Equilibrium Internal Coordinates for TNAZ[a]

Bond	Value (Å)	Angle	Value (deg.)	Torsion	Value (deg.)
r_{N1C2}	1.481	θ_{C2N1C4}	93.971	$\tau_{N1C2C3N7}$	126.191
r_{C2C3}	1.542	θ_{C2N1N5}	118.393	$\tau_{N6C3C4N1}$	108.506
r_{C3C4}	1.542	θ_{C4N1N5}	118.387	$\tau_{C2N1N5O9}$	- 35.065
r_{N1C4}	1.481	θ_{N1C2C3}	87.648	$\tau_{C4N1N5O8}$	35.069
r_{N1N5}	1.397	$\theta_{N1C2H14}$	112.942	$\tau_{C4C3N6O10}$	- 141.378
r_{C3N6}	1.514	$\theta_{N1C2H15}$	114.873	$\tau_{C2C3N6O11}$	140.372
r_{C3N7}	1.523	$\theta_{C3C2H14}$	113.182	$\tau_{C2C3N7O12}$	- 50.638
r_{N5O8}	1.225	$\theta_{C3C2H15}$	115.157	$\tau_{C4C3N7O12}$	- 129.374
r_{N5O9}	1.225	$\theta_{H14C2H15}$	111.233	$\tau_{C2N1C4H17}$	104.656
r_{N6O10}	1.223	θ_{C2C3C4}	89.194	$\tau_{C2N1C4H16}$	126.316
r_{N6O11}	1.222	θ_{C2C3N6}	115.229	$\tau_{C4N1C2H14}$	104.65
r_{N7O12}	1.219	θ_{C2C3N7}	114.750	$\tau_{C4N1C2H15}$	- 126.317
r_{N7O13}	1.224	θ_{C4C3N6}	115.211		
r_{C2H14}	1.092	θ_{C4C3N7}	114.732		
r_{C2H15}	1.089	θ_{N6C3N7}	107.247		
r_{C4H16}	1.090	θ_{N1C4C3}	87.648		
r_{C4H17}	1.092	$\theta_{N1C4H16}$	114.866		
		$\theta_{N1C4H17}$	112.937	Wag	Value (deg.)
		$\theta_{C3C4H16}$	115.157		
		$\theta_{C3C4H17}$	113.186	$\gamma_{C2N1C4N5}$	45.815
		$\theta_{H16C4H17}$	111.240	$\gamma_{C2C3C4N6}$	53.245
		θ_{N1N5O8}	115.891	$\gamma_{C2C3C4N7}$	- 54.002
		θ_{N1N5N9}	115.894		
		θ_{O8N5O9}	128.156		
		$\theta_{C3N6O10}$	116.346		
		$\theta_{C3N6O11}$	116.335		
		$\theta_{O10N6O11}$	127.319		
		$\theta_{C3N7O12}$	118.123		
		$\theta_{C3N7O13}$	114.535		
		$\theta_{O12N7O13}$	127.342		

[a] See Figure 3 for atomic assignments.

Table VIII. Equilibrium Geometry for TNAZ

Atomic Label[a]	Cartesian Coordinates (Å)		
	x	y	z
N_1	1.33416109	-0.68079525	-0.00025104
C_2	0.42079401	-0.24972575	-1.08293584
C_3	-0.65446700	-0.02513046	-0.00031654
C_4	0.42044800	-0.24890132	1.08281769
N_5	2.64278832	-0.19067132	0.00036971
N_6	-1.78875489	-1.02746656	0.00017773
N_7	-1.27933144	1.36399971	-0.00063766
O_8	3.15198499	-0.02587919	1.10182807
O_9	3.15247994	-0.02652683	-1.10095501
O_{10}	-2.20123311	-1.38054185	-1.09513312
O_{11}	-2.18846509	-1.39359817	1.09593575
O_{12}	-2.49510393	1.44696669	-0.00090557
O_{13}	-0.47229932	2.28439077	-0.00055751
H_{14}	0.74203272	0.67447044	-1.56806415
H_{15}	0.18514547	-1.01945622	-1.81709863
H_{16}	0.18461583	-1.01816044	1.81741544
H_{17}	0.74163766	0.67564157	1.56731752

[a] See Figure 3 for atomic assignments.

Table IX. Equilibrium Internal Coordinates for 13DNAZ[a]

Bond	Value (Å)	Angle	Value (deg.)	Torsion	Value (deg.)
r_{N1C2}	1.496	θ_{C2N1C4}	93.785	$\tau_{C2C3N6O10}$	168.323
r_{C2C3}	1.492	θ_{C2N1N5}	117.847	$\tau_{C4N1N5O7}$	35.792
r_{C3C4}	1.492	θ_{C4N1N5}	117.847	$\tau_{N1C4C3N6}$	-156.342
r_{N1C4}	1.496	θ_{N1C2C3}	85.765	$\tau_{C3C2N1N5}$	130.026
r_{N1N5}	1.400	$\theta_{N1C2H11}$	112.849		
r_{C3N6}	1.397	$\theta_{N1C2H12}$	114.298		
r_{N5O7}	1.225	$\theta_{C3C2H11}$	116.449		
r_{N5O8}	1.225	$\theta_{C3C2H12}$	116.777		
r_{N6O9}	1.242	$\theta_{H11C2H12}$	109.148		
r_{N6O10}	1.242	θ_{C2C3C4}	94.124		
r_{C2H11}	1.097	θ_{C2C3N6}	131.511		
r_{C2H12}	1.094	θ_{C4C3N6}	131.511		
r_{C4H13}	1.094	θ_{N1C4C3}	85.765		
r_{C4H14}	1.097	$\theta_{N1C4H13}$	114.298		
		$\theta_{N1C4H14}$	112.849		
		$\theta_{C3C4H13}$	116.777		
		$\theta_{C3C4H14}$	116.449		
		$\theta_{H13C4H14}$	109.148	Wag	Value (deg.)
		θ_{N1N5O7}	116.068		
		θ_{N1N5O8}	116.068	$\gamma_{C2N1C4N5}$	47.124
		θ_{O7N5O8}	127.789	$\gamma_{C2C3C4N6}$	17.228
		θ_{C3N6O9}	116.857		
		$\theta_{C3N6O10}$	116.857		
		$\theta_{O9N6O10}$	126.280		

[a] See Figure 4 for atomic assignments.

Table X. Equilibrium Geometry for 13DNAZ

	Cartesian Coordinates (Å)		
Atomic Label[a]	x	y	z
N_1	0.99047416	-0.00008725	0.55473083
C_2	0.05274837	-1.09163595	0.14609622
C_3	-0.92892236	0.00002228	-0.12778747
C_4	0.05274647	1.09159361	0.14645464
N_5	2.27705521	0.00000358	-0.00700912
N_6	-2.33402117	0.00001522	-0.08782443
O_7	2.77769025	1.09677084	-0.19653059
O_8	2.77769362	-1.09677084	-0.19653059
O_9	-2.89022294	-1.10395870	-0.08079918
O_{10}	-2.89026996	1.10397084	-0.08150581
H_{11}	0.41543105	-1.66373488	-0.72555817
H_{12}	-0.20886319	-1.79365826	0.95325437
H_{13}	-0.20886994	1.79334970	0.95383695
H_{14}	0.41542697	1.66397458	-0.72501722

[a] See Figure 4 for atomic assignments.

Table XI. Equilibrium Internal Coordinates for 33DNAZ

Bond	Value (Å)	Angle	Value (deg.)	Torsion	Value (deg.)
r_{N1C2}	1.477	θ_{C2N1C4}	90.103	$\tau_{C4C3N6O10}$	49.200
r_{C2C3}	1.538	θ_{N1C2N3}	91.932	$\tau_{C2C3N5O8}$	139.144
r_{C3C4}	1.538	$\theta_{N1C2H11}$	112.062	$\tau_{N1C4C3N6}$	121.683
r_{N1C4}	1.477	$\theta_{N1C2H12}$	114.421	$\tau_{N1C2C3N5}$	-111.781
r_{C3N5}	1.512	$\theta_{C3C2H11}$	113.435		
r_{C3N6}	1.521	$\theta_{C3C2H12}$	115.017		
r_{N5O7}	1.224	$\theta_{H11C2H12}$	109.203		
r_{N5O8}	1.224	θ_{C2C3C4}	85.595		
r_{N6O9}	1.220	θ_{C2C3N5}	115.876		
r_{N6O10}	1.225	θ_{C2C3N6}	115.934		
r_{C2H11}	1.096	θ_{C4C3N5}	115.891		
r_{C2H12}	1.095	θ_{C4C3N6}	115.916		
r_{C4H13}	1.095	θ_{N5C3N6}	106.921		
r_{C4H14}	1.096	θ_{N1C4C3}	91.931		
		$\theta_{N1C4H13}$	114.420		
		$\theta_{N1C4H14}$	112.064		
		$\theta_{C3C4H13}$	115.009		
		$\theta_{C3C4H14}$	113.445	Wag	Value (deg.)
		$\theta_{H13C4H14}$	109.202		
		θ_{C3N5O7}	116.460	$\gamma_{C2C3C4N5}$	57.264
		θ_{C3N5O8}	116.483	$\gamma_{C2C3C4N6}$	-54.807
		θ_{O7N5O8}	127.055		
		θ_{C3N6O9}	118.511		
		$\theta_{C3N6O10}$	114.581		
		$\theta_{O9N6O10}$	126.909		

[a] See Figure 5 for atomic assignments.

Table XII. Equilibrium Geometry for 33DNAZ

Atomic Label[a]	Cartesian Coordinates (Å)		
	x	y	z
N_1	1.85125410	-1.62151253	0.00018772
C_2	1.06765107	-0.92457186	-1.05059891
C_3	0.21996954	-0.17061354	-0.01048211
C_4	1.08628246	-0.94111995	1.06332462
N_5	-1.26763171	-0.45590756	-0.01278821
N_6	0.33805328	1.35048808	-0.01283927
O_7	-1.78866342	-0.60817471	-1.10441337
O_8	-1.80960459	-0.51651815	1.07757710
O_9	-0.68103388	2.00929629	-0.07717656
O_{10}	1.48356328	1.76813146	0.05162694
H_{11}	1.69978539	-0.26636653	-1.66992853
H_{12}	0.49829910	-1.597338035	-1.71191719
H_{13}	0.51689649	-1.62028689	1.71807990
H_{14}	1.72414359	-0.28262455	1.67644486

[a] See Figure 5 for atomic assignments.

Table XIII. Equilibrium Geometry for NO_2

	Cartesian Coordinates (Å)		
Atomic Label	x	y	z
N_1	-0.23325183	1.35483339	0.90605149
O_2	-0.30939681	-0.23340550	-0.15755942
O_3	0.51359749	-0.95268553	-0.63564479

Table XIV. Potential Parameters for TNAZ

Morse Parameters:

Bond	De (kcal/mol)[74]	α ($Å^{-1}$)
r_{N1N5}	46.6	3.48958
r_{C3N6}	44.6	3.93964
r_{C3N7}	44.6	3.93964

Harmonic Bond Force Constants:

Bond		k_r (kcal mol^{-1} $Å^{-2}$)
r_{N1C2}	1	546.6056
r_{C2C3}	2	653.5103
r_{C3C4}	3	651.2119
r_{N1C4}	4	541.3949
r_{N5O8}	5	834.1971
r_{N5O9}	6	834.1971
r_{N6O10}	7	825.2446
r_{N6O11}	8	825.2446
r_{N7O12}	9	825.2446
r_{N7O13}	10	825.2446
r_{C2H14}	11	766.3881
r_{C2H15}	12	766.4725
r_{C4H16}	13	767.6548
r_{C4H17}	14	767.5703

Harmonic Angle Force Constants:

Angle	k_θ (kcal mol^{-1} rad^{-2})
θ_{C2N1C4}	138.0523
θ_{C2N1N5}	213.0701
θ_{C4N1N5}	213.0701
θ_{N1C2C3}	206.0752
$\theta_{N1C2H14}$	101.0248
$\theta_{N1C2H15}$	101.0248
$\theta_{C3C2H14}$	93.9517
$\theta_{C3C2H15}$	93.9517
$\theta_{H14C2H15}$	33.7089
θ_{C2C3C4}	210.2615
θ_{C2C3N6}	213.0231
θ_{C2C3N7}	213.0231
θ_{C4C3N6}	213.0231
θ_{C4C3N7}	213.0231
θ_{N6C3N7}	348.6424

Table XIX. Continued

Angle	k_θ (kcal mol^{-1} rad^{-2})
θ_{N1C4C3}	206.0752
$\theta_{N1C4H16}$	101.0248
$\theta_{N1C4H17}$	101.0248
$\theta_{C3C4H16}$	93.9517
$\theta_{C3C4H17}$	93.9517
$\theta_{H16C4H17}$	33.7089
θ_{N1N5O8}	209.8721
θ_{N1N5N9}	209.8721
θ_{O8N5O9}	443.0023
$\theta_{C3N6O10}$	210.2885
$\theta_{C3N6O11}$	210.2558
$\theta_{O10N6O11}$	443.0023
$\theta_{C3N7O12}$	210.2885
$\theta_{C3N7O13}$	210.2885
$\theta_{O12N7O13}$	443.0023

Harmonic Wag Force Constants:

Angle	k_γ (kcal mol^{-1} rad^{-2})
$\gamma_{C2N1C4N5}$	15.0000
$\gamma_{C2C3C4N6}$	15.0000
$\gamma_{C2C3C4N7}$	15.0000

Torsional Fourier Coefficients:

Angle	a_0	a_2	a_4
$\tau_{N1C2C3N7}$	1.952326	1.997644	1.650012
$\tau_{N6C3C4N1}$	9.410194	13.210308	4.135967
$\tau_{C2N1N5O9}$	2.364518	- 2.611294	1.920713
$\tau_{C4N1N5O8}$	2.363904	- 2.610019	1.920508
$\tau_{C4C3N6O10}$	1.960004	- 1.577234	1.785884
$\tau_{C2C3N6O11}$	1.882353	- 1.312525	1.760000
$\tau_{C2C3N7O12}$	1.901424	1.381578	1.766346
$\tau_{C4C3N7O12}$	1.900549	1.378477	1.766055
$\tau_{C2N1C4H17}$	8.254474	11.421868	3.274768
$\tau_{C2N1C4H16}$	1.015287	1.028948	0.861706
$\tau_{C4N1C2H14}$	8.257959	11.426558	3.275930
$\tau_{C4N1C2H15}$	1.015200	1.028738	0.861677
$\tau_{N1C4C3N7}$	1.855974	1.896724	1.569442
$\tau_{N6C3C2N1}$	8.298402	11.648965	3.645644

Table XV. Potential Parameters for 13DNAZ

Harmonic Bond Force Constants:

Bond		k_r (kcal mol^{-1} Å^{-2})
r_{N1C2}	1	542.2885
r_{C2C3}	2	652.5623
r_{C3C4}	3	651.4495
r_{N1C4}	4	540.6247
r_{N5O7}	5	835.5199
r_{N5O8}	6	835.5060
r_{N6O9}	7	830.9471
r_{N6O10}	8	830.9888
r_{C2H11}	9	765.6371
r_{C2H12}	10	765.9739
r_{C4H13}	11	765.9587
r_{C4H14}	12	765.0024

Harmonic Angle Force Constants:

Angle	k_θ (kcal mol^{-1} rad^{-2})
θ_{C2N1C4}	140.1739
θ_{C2N1N5}	205.6473
θ_{C4N1N5}	205.6125
θ_{N1C2C3}	210.1623
$\theta_{N1C2H11}$	98.5091
$\theta_{N1C2H12}$	98.3192
$\theta_{C3C2H11}$	95.4178
$\theta_{C3C2H12}$	95.6656
$\theta_{H11C2H12}$	36.6835
θ_{C2C3C4}	210.4016
θ_{C2C3N6}	215.4069
θ_{C4C3N6}	215.9473
θ_{N1C4C3}	210.8400
$\theta_{N1C4H13}$	98.4705
$\theta_{N1C4H14}$	98.0832
$\theta_{C3C4H13}$	93.8979
$\theta_{C3C4H14}$	93.7579
$\theta_{H13C4H14}$	36.8664
θ_{N1N5O7}	210.9289
θ_{N1N5N8}	210.1419
θ_{O7N5O8}	440.2516
θ_{C3N6O9}	215.7185
$\theta_{C3N6O10}$	215.4407
$\theta_{O9N6O10}$	440.1875

Table XV. Continued

Harmonic Wag Force Constants:

Angle	k_γ (kcal mol^{-1} rad^{-2})
$\gamma_{C2N1C4N5}$	15.0000
$\gamma_{C2C3C4N6}$	15.0000

Torsional Fourier Coefficients:

Angle	a_0	a_2	a_4
$\tau_{C2C3N6O10}$	16.614211	-22.717114	6.186921
$\tau_{C4N1N5O7}$	9.928124	-10.458321	8.276287
$\tau_{N1C4C3N6}$	8.601046	-12.153063	4.479898
$\tau_{C3C2N1N5}$	13.510858	8.808453	12.749928

Table XVI. Potential Parameters for 33DNAZ

Harmonic Bond Force Constants:

Bond		k_r (kcal mol^{-1} Å^{-2})
r_{N1C2}	1	540.9252
r_{C2C3}	2	652.2271
r_{C3C4}	3	651.1714
r_{N1C4}	4	543.9858
r_{N5O7}	5	833.8295
r_{N5O8}	6	833.8594
r_{N6O9}	7	833.3958
r_{N6O10}	8	833.4773
r_{C2H11}	9	766.6122
r_{C2H12}	10	766.8231
r_{C4H13}	11	766.7999
r_{C4H14}	12	766.1107

Harmonic Angle Force Constants:

Angle	k_θ (kcal mol^{-1} rad^{-2})
θ_{C2N1C4}	140.1595
θ_{N1C2C3}	210.6465
$\theta_{N1C2H11}$	99.7901
$\theta_{N1C2H12}$	99.5960
$\theta_{C3C2H11}$	100.5621
$\theta_{C3C2H12}$	100.2834
$\theta_{H11C2H12}$	34.3484
θ_{C2C3C4}	210.4420
θ_{C2C3N5}	215.4070
θ_{C2C3N6}	215.5914
θ_{N5C3N6}	281.7756
θ_{C4C3N6}	215.2677
θ_{C4C3N5}	215.1841
θ_{N1C4C3}	210.2573
$\theta_{N1C4H13}$	99.4917
$\theta_{N1C4H14}$	99.6310
$\theta_{C3C4H13}$	100.9728
$\theta_{C3C4H14}$	100.4087
$\theta_{H13C4H14}$	34.6824
θ_{C3N5O7}	213.9877
θ_{C3N5O8}	212.8562
θ_{O7N5O8}	440.8948
θ_{C3N6O9}	212.4869
$\theta_{C3N6O10}$	213.3048
$\theta_{O9N6O10}$	441.2488

Table XVI. Continued

Harmonic Wag Force Constants:

Angle	k_γ (kcal mol^{-1} rad^{-2})
$\gamma_{C2N1C4N5}$	15.0000
$\gamma_{C2C3C4N6}$	15.0000

Torsional Fourier Coefficients:

Angle	a_0	a_2	a_4
$\tau_{C4C3N6O10}$	16.08095	10.77680	18.44296
$\tau_{C2C3N5O8}$	51.55450	- 28.53830	49.49623
$\tau_{N1C4C3N6}$	26.64269	34.07663	19.00374
$\tau_{N1C2C3N5}$	318.2917	450.0962	156.3337

Table XVII. Comparison of TNAZ Normal Mode Frequencies (cm^{-1})

PES[a]	Gas Phase[43]	scaled B3LYP[a]	Solid[104]	Matrix[41]
33 (7)		**26**		
60(18)		**42**		
97(21)		**76**		
98(18)	**80**	97		
175(13)	**162**	150		
456(24)	**480**	174		
497(17)	**480**	224		
532(32)	**564**	260		
533(31)	**564**	288		
552(12)	**564**	330		
586(15)	**601**	356		
605(11)	**626**	400		
615(11)	**626**	502		
606(20)	**626**	524		
658 (4)	**662**	586		
665 (3)	**662**	639		
712 (0)	**712**	692		
819 (3)	**816**	694		658
842 (1)	**843**	742		
848 (5)	**843**	791	762	
860 (7)	**865**	818	815	
863 (2)	**865**	836	844	
905 (1)	**906**	883	867	817
1059 (2)	**1057**	912	908	841
1063 (6)	**1057**	1022		865
1087 (2)	**1085**	1067		906
1117 (4)	**1113**	1086		1040
1172 (0)	**1172**	1102	1088	1091
1183 (0)	**1183**	1138	1115	1123
1199 (1)	**1200**	1147	1175	1159
1219 (3)	**1216**	1180	1184	
1279 (1)	**1280**	1227	1219	1207
1327 (2)	**1325**	1255	1282	1215
1342 (2)	**1340**	1323		1277
1364 (1)	**1365**	1329	1328	1325
1380 (0)	**1380**	1372	1340	1330
1401 (2)	**1403**	1434	1367	1363
1431 (3)	**1428**	1454	1382	1442
1615 (3)		**1618**	1410	1459
1629 (4)		**1625**	1427	1586
1632 (4)		**1628**	1590	1593
2900 (0)	**2900**	2986	2919	2907
2973 (0)	**2973**	2991	2976	2979
3021 (0)	**3021**	3059	3022	
3036 (0)	**3036**	3059	3037	3028

Frequencies in bold type font are those which the equilibrium potential energy surface was fit. [a] This work.

Table XVIII. Product Fragments Normal Mode Frequencies (cm^{-1})

13DNAZ		33DNAZ		NO_2	
PES[a]	B3LYP[b]	PES[a]	B3LYP[b]	PES[a]	B3LYP[b]
68 (14)	54	29 (8)	21	70 (14)	56
78 (6)	72	57 (3)	54	70 (14)	56
140 (24)	116	85 (10)	75	141 (24)	117
153 (9)	144	181 (7)	188		
189 (15)	174	222 (11)	233		
221 (41)	262	241 (9)	250		
269 (36)	305	263 (34)	297		
336 (39)	375	360 (18)	378		
481 (29)	510	398 (19)	417		
493 (38)	531	469 (28)	497		
503 (77)	580	543 (77)	620		
557 (89)	646	582 (89)	671		
707 (39)	746	715 (39)	676		
724 (44)	768	723 (44)	767		
767 (31)	798	772 (31)	803		
859 (39)	820	844 (17)	827		
910 (17)	893	858 (24)	834		
965 (5)	970	888 (5)	883		
1011 (4)	1015	960 (4)	956		
1025 (11)	1036	1008 (11)	997		
1081 (6)	1075	1032 (6)	1026		
1092 (3)	1095	1091 (3)	1094		
1160 (7)	1167	1093 (9)	1102		
1172 (6)	1178	1169 (8)	1177		
1227 (7)	1234	1200 (5)	1205		
1295 (25)	1270	1259 (4)	1255		
1299 (14)	1313	1315 (16)	1331		
1344 (9)	1353	1373 (8)	1365		
1379 (33)	1412	1406 (29)	1377		
1395 (37)	1432	1369 (30)	1399		
1517 (51)	1466	1597 (21)	1618		
1623 (11)	1612	1629 (9)	1620		
2927 (4)	2931	2934 (1)	2935		
2927 (12)	2939	2926 (14)	2940		
2979 (10)	2989	2979 (14)	2993		
2980 (10)	2990	2980 (14)	2994		

[a] Frequencies for the equilibrium PES's were fit to the scaled *ab initio* frequencies.
[b] Scaled *ab initio* B3LYP/6-31G(d,p) frequencies. Numbers in parentheses are absolute error between the fit and *ab initio* frequencies.

Table XIX. Comparison of TNAZ *Ab Initio* and Experimental Frequencies (cm^{-1})

Freq. No.[a]	B3LYP[b]	Exp.[c]	Scaling[d]
25	1062.8	1056.7	0.9942
26	1109.7	1085.1	0.9778
27	1129.6	1112.7	0.9850
28	1145.8	1171.9	1.0227
29	1183.3	1182.6	0.9994
30	1193.6	1200.0	1.0054
31	1227.5	1216.1	0.9907
32	1276.2	1280.0	1.0030
33	1305.4	1324.9	1.0150
34	1376.2	1340.4	0.9740
35	1382.6	1365.0	0.9873
36	1426.9	1379.6	0.9668
37	1491.7	1403.3	0.9407
38	1512.1	1428.2	0.9445
42	3105.8	2900.2	0.9338
43	3110.9	2973.1	0.9557
44	3181.8	3020.5	0.9493
45	3181.8	3035.8	0.9541

[a] These frequencies were chosen due to a clearer correspondence between the experimental and computed values. [b] Un-scaled *ab initio* frequencies.
[c] Experimental frequencies of Yu *et al.*[43].
[d] The scaling factor between the *ab initio* and experimental frequencies.

Table XX. Comparison of Calculated to Experimental Rates

Energy (kcal/mol)	calc. k (ps^{-1})[a]	exper. k (ps^{-1})[b]	temp (K)[c]	error magnitude
250	0.01312	0.05779	2702	4.40
300	0.05847	0.2099	3277	3.59
350	0.1851	0.5163	3847	2.79
400	0.3186	1.009	4415	3.17
450	0.5244	1.680	4981	3.20
500	0.8919	2.532	5545	2.84
550	1.242	3.522	6108	2.84
600	1.855	4.613	6671	2.49
650	2.310	5.807	7233	2.51
700	3.000	7.100	7795	2.37

[a] Calculated rate as determined in this work.
[b] Extrapolated experimental rates of Zhang and Bauer[33].
[c] The experimental range was 750 – 1100K. The temperature was extrapolated using Equation 31.

Table XXI. Branching Ratios for Dissociation of TNAZ

Energy	k_2(N-NO_2)	k_3(C-NO_2)	k_4(C-NO_2)$_{ax}$	k_5(C-NO_2)$_{eq}$	k_2:k_3	k_4:k_5
250	0.006256[a]	0.006869	0.003551	0.003317	0.911	1.07
300	0.02856	0.02991	0.01361	0.01630	0.955	0.835
350	0.08220	0.1029	0.05443	0.04851	0.799	1.12
400	0.1396	0.1791	0.08188	0.09717	0.779	0.843
450	0.2344	0.2900	0.1343	0.1558	0.808	0.862
500	0.3559	0.5360	0.2586	0.2774	0.664	0.932
550	0.5332	0.7085	0.3393	0.3692	0.753	0.919
600	0.7996	1.056	0.5176	0.5380	0.757	0.962
650	0.9827	1.327	0.6798	0.6474	0.740	1.05
700	1.266	1.734	0.8011	0.9331	0.730	0.859

[a] All rates are in ps^{-1}.

PART TWO

CHAPTER V

CONCLUSIONS AND FUTURE WORK

As stated in the introduction of Part Two, the goal of this work was to develop a reactive potential energy surface that would accurately predict the unimolecular dissociation rate of TNAZ. The switched reactive potential for the unimolecular dissociation of TNAZ predicts the rate within the experimental error of Reference 33 as shown in Figure 16. This is the case for extrapolated experimental data. The trend tends to deviate from the extrapolated experimental region as the temperature decreases indicating that the rate is underestimated at some point in the experimental range. This is shown by using the vibrational energy partition function to extrapolate experimental data into the computed region to be more accurate than using $k_B T$ approximation. The switched potential energy surface may not consider all the internal IVR pathways leading to dissociation. The transition state configuration of TNAZ has been determined lending itself to further study using variational transition state theory (VTST). The IVR study may indicate participating modes for dissociation i.e. 'hot' and 'cold' modes responsible for R-NO_2 scission.

As energy is increased C-NO_2 scissions are slightly favored over N-NO_2. The

branching ratio of C-NO_2(axial) and C-NO_2(equatorial) shows no energy dependence (see Table XXI and Figure 13). In preliminary IVR work the flow of energy favors the C-NO_2 modes. More detailed work is needed to completely characterize the IVR in TNAZ.

Future characterization of the dissociation of TNAZ could be reasonably predicted with similar switched potential energy surfaces and experimentally given reaction paths. One avenue of interest would be to prepare a switched potential where all known reaction paths are considered, not just the N-NO_2 scissions. Future IVR work could also help with predictions of energy flow and help validate reaction pathways. It is hoped that the current PES can be used in similar nitramines.

REFERENCES

1. D. Bedrov, C. Ayyagari, G. D. Smith, T. D. Sewell, R. Menikoff, J. M. Zaug, *J. Computer-Aided Mat. Des.* **8**, 77 (2002).
2. G. D. Smith, R. K. Bharadwaj, *J. Phys. Chem. B,* **103**, 3570, (1999).
3. M. M. Kuklja, F. J. Zerilli, S. M. Peiris, *J. Chem. Phys.,* **118**, 11073 (2003).
4. J. J. Haycraft, L. L. Stevens, C. J. Eckhardt, *J. Chem. Phys.*, **124**, 24712, (2006).
5. R. B. Schwarz, D. E. Hooks, J. J. Dick, J. I. Archuleta, A. R. Martinez, *J. Appl. Phys.,* **98**, 056106, (2005).
6. S. Haussühl, *Z. Kristallogr.,* **216**, 335 (2001).
7. Y. Zhou, M. A. Baseer, H. Mahfuz, S. Jeelani, *Mat. Science and Eng. A.*, **420**, 63 (2006).
8. T. Goldmann, H. Seiner, M. Landa, *Technology and Health Care Official Journal of the European Society for Engineering and Medicine,* **14**, 219 (2006).
9. J. P. Marquez, G. M. Genin, G. I. Zahalak, E. L. Elson, *Biophysical Journal,* **88**, 765 (2005).
10. S. Ulam, *Los Alamos Science,* **15**, (1987).
11. J. P. Valleau, G. M. Torrie, in *Modern Theoretical Chemistry*, ed. B. J. Berne (Plenum, New York, 1977).
12. J. D. Doll, D. L. Freeman, T. L. Beck, *Adv. Chem. Phys.* **78**, 61 (1990).

13. D. Ceperley, *Rev. Mod. Phys.* **67**, 279 (1995).

14. J. D. Doll, D. L. Freeman in *Modern Methods for Multidimensional Dynamics Computations in Chemistry*, ed. D. L. Thompson (World Scientific, New Jersey, 1998).

15. W. W. Wood, in *Physics of Simple Fluids*, edited by H. N. V. Temperley, J. S. Rowlinson and G. S. Rushbrooke (North-Holland, Amsterdam, 1968), Chap. 5, p. 115.

16. M. Parrinello and A. Rahman, J Appl. Phys. **52**, 7182 (1981).

17. S. Yashonath and C. N. R. Rao, Mol. Phys. **54**, 245 (1985).

18. N. Metropolis, A. W. Rosenbluth M. N. Rosenbluth, A. H. Teller and E. Teller, J. Chem. Phys. **21**, 1087 (1953).

19. D. C. Sorescu, B. M. Rice and D. L. Thompson, J. Phys. Chem. B **101**, 798 (1997).

20. D. E. Williams and S. R. Cox, Acta Crystallogr., Sect. B: Struct. Sci. **40**, 404 (1984).

21. S. R. Cox, L. Y. Hsu and D. E. Williams, Acta Crystallogr., Sect. A: Cryst. Phys., Diffr., Theor. Gen. Crystallogr., **37**, 293 (1981).

22. A. J. Pertsin and A. I. Kitaigorodsky, *The Atom-Atom Potential Method. Applications to Organic Molecular Solids* (Springer, Berlin, 1987).

23. S. L. Price, in *Review in Computational Chemistry*, edited by K. B. Lipkowitz and D. B. Boyd (Wiley-VCH, New York, 1999), Vol. 14, p. 225.

24. G. D. Smith and R. K. Bharadwaj, J. Phys. Chem. B **103**, 3570 (1999).

25. D. C. Sorescu, B. M. Rice and D. L. Thompson, J. Phys. Chem. B **102**, 6692 (1998).

26. H. H. E. Leipholz, *Theory of Elasticity* (Noordhoff, Leyden, 1974).

27. M. Parrinello and A. Rahman, J. Chem. Phys. **76**, 2662 (1982).

28. S. W. Tsai, AFML Techncal Report No. AFML-TR-66-149, November, 1966.

29. C. S. Choi and E. Prince, Acta Crystallogr., Sect. B: Struct. Crystallogr. Cryst. Chem. **28**, 2857 (1972).

30. A. Hald, in *Statistical Theory with Engineering Applications* (Wiley, New York, 1952) Chap. 13, p. 338.

31. T. D. Sewell, J. Appl. Phys. **83**, 4142 (1998).

32. B. Olinger, B. Roof and H. Cady, Symposium International Sur le Comportement Des Milieux Denses Sous Hautes Pressions Dynamiques. Paris, France, 1978, p. 3.

33. Y.-X. Zhang and S. H. Bauer, *J.Phys. Chem. A*, **102**, 5846, (1998).

34. T. G. Archibald, R. Gilardi, K. Baum, *et al., J. Org. Chem.,* **55**, 2920 (1990).

35. S. Iyer, Y. S. Eng, M. Joyce, R. Perez, J. Alster, and D. Stec, in *Proceedings of the Joint International Symposium on Compatibility of Plastics and Other Materials with Explosives, Propellants, Pyrotechnics and Processing of Explosives, Propellants and Ingredients,* 1991, pp. 80-84.

36. L. B. Piper and J. D. Filliben, "New High-Energy Oxidizers CPIA Report", (1993).

37. G. A. Crowder *et al.*, *J. Energetic. Mat.,* **17**, 49 (1999).

38. R. L. McKenney, W. E. Stevens, and T. G. Floyd, *J. Energetic Mat.*, **17**, 113 (1999).

39. E. Tannenbaum, R. J. Myers, and W. D. Gwinn, *J. Chem. Phys.*, **25**, 42 (1956).

40. J. Ekkers, A. Bauder, and H. Gunthard, *Chem. Phys. Lett.,* **22**, 249 (1973).

41. C. A. Thompson, J. K. Rice, T. P. Russell, J. M. Seminario, and P. Politzer, *J. Phys. Chem. A,* **101**, 7742, (1997).

42. C. Lee, W. Yang and R. G. Parr, *Phys. Rev. B: Condens. Matter,* **41**, 785 (1988).

43. C. L. Yu, Y. X. Zhang and S. H. Bauer, *J. Mol. Struct. (THEOCHEM),* **432**, 63 (1998).

44. J. Oxley, J. Smith, W. Zheng, E. Rogers, and M. Coburn, *J. Phys. Chem. A*, **101**, 4375 (1997).

45. J. Oxley, A. B. Kooh, R. J. Szekeres, and W. Zheng, *J. Phys. Chem.,* **98**, 7004 (1994).

46. K. Anderson, J. Homsey, and R. Behrens in *Modeling the thermal Decomposition of TNAZ and NDNAZ,* Snow Mass, CO (2000).

47. S. Bulusu and J. R. Behrens, *Def. Science Journal*, **46**, 347 (1996).

48. R. Behrens in *Chemistry and Physics of Energetic Materials; Vol. 309*, edited by S. Bulusu (Kluwer Academic Publishers, Netherlands, 1990), p. 327.

49. R. Behrens, *Rev. Sci. Instrum.,* **58**, 451 (1986).

50. R. Behrens, *J. Phys. Chem.,* **94**, 6706 (1990).

51. R. Behrens and S. Bulusu, *J. Phys. Chem.,* **95**, 5838 (1991).

52. R. Behrens and S. Bulusu, *J. Phys. Chem.,* **96**, 8877 (1992).

53. R. Behrens and S. Bulusu, *J. Phys. Chem.,* **96**, 8891 (1992).

54. N. L. Garland and H. H. Nelson, *J. Phys. Chem. B,* **102**, 2663 (1998).

55. N. L. Garland, H. D. Landouceur and H. H. Nelson, *J. Phys. Chem. A*, **101**, 8508 (1997).

56. D. F. McMillen, E. C. Erlich, C. He, C. H. Becker and D. Shockley, *Combustion and Flame*, **111** (1989).

57. S. E. Nigenda, D. F. McMillen and D. M. Golden, *J. Phys. Chem.,* **93**, 1124 (1989).

58. W. Zhen, E. Rogers, M. Coburn, J. Oxley and J. Smith, *J. Mass. Spec.*, **32**, 525 (1997).

59. Y. Oyumi and T. B. Brill, *Combustion and Flame*, **62**, 225 (1985).

60. Y. Oyumi and T. B. Brill, *Combustion and Flame*, **68**, 209 (1987).

61. D. S. Anex, J. C. Allman and Y. T. Lee in *Chemistry of Energetic Materials,* editied by G. A. Olah and D. R. Squire (Academic Press, New York, 1991), pp. 27-54.

62. C. F. Wilcox, Y. –X. Zhang and S. H. Bauer, *J. Molecular Struct. (THEOCHEM)* **528**, 95 (2000).

63. *Computational Thermochemistry*, edited by M. R. Zachariah, C. F. Melius, K. K. Irikura and D. J. Frurip (American Chemical Society, Washington DC, 1998).

64. A. A. Porollo, T. V. Petukhova, V. P. Ivshin, T. S. Pivina and D. E. Lushnikov in *Azetidine and its mono-, di-, and tri-nitrosubstituted derivatives: Computer modeling of decomposition reactions*, 1999, pp. 15.1 – 15.13.

65. M. J. S. Dewar, E. F. Healy, A. J. Holder and Y. C. Yuan, *J. Comp. Chem.*, **11**, 541 (1990).

66. Z. Jiaoqiang, Z. Chunhua, G. Xuedong and X. Heming, *Wuli Huaxue Xuebao*, **13**, 612 (1997).

67. Y. –X. Zhang and S. H. Bauer, *International J. Chem. Kinetics*, **31**, 655 (1999).

68. C. F. Melius in *Chemistry and Physics of Energetic Materials*, edited by S. Bulusu (Kluwer Academic Publishers, Boston, MA, 1990).

69. T. Miyauchi, Y. Mori and A. Imamura in *Sixteenth Symposium (International) on Combustion* (The Combustion Institute, Pittsburgh, 1976), p. 4073.

70. R. A. Cox, *J. Photochem.*, **3**, 175 (1974).

71. W. Tsang and R. F. Hampson, *J. Phys. Ref. Data*, **15**, 1087 (1987).

72. W. Tsang, M. C. Lin and C. F. Melius, *J. Chem. Kin.* **22**, 455 (1990).

73. A. F. Podonov *et al.*, *Kinetics and Catalysis*, **22**, 689 (1981).

74. J. P. Reilly *et al., J. Phys. Chem.*, **69**, 4381 (1978).

75. F. Stoeckel, *Chem. Phys.*, **95**, 135 (1985).

76. A. Szekely, R. K. Hanson and C. T. Bowman, *Int. J. Chem. Kin.*, **16**, 1609 (1984).

77. P. Politzer and J. M. Seminario, *Chem. Phys. Lett.*, **207**, 27 (1993).

78. J. M. Seminario and P. Politzer, *Int. J. Quant. Chem. Symp.* **26**, 497 (1992).

79. A. D. Becke, *J. Chem. Phys.*, **84**, 4524 (1986).

80. T. Ziegler, V. Tschinke and A. D. Becke, *J. Amer. Chem. Soc.*, **109**, 1351 (1987).

81. T. Ziegler, *Chem. Rev.*, **91**, 651 (1991).

82. L. Fan and T. Ziegler, *J. Chem. Phys.*, **94**, 6057 (1991).

83. P. Politzer, P. Lane, M. E. Grice, M. C. Concha and P. C. Redfern, *J. Mol. Struct. (THEOCHEM)*, **338**, 248 (1995).

84. D. C. Sorescu, C. M. Bennett and D. L. Thompson, *J. Phys. Chem. A,* **102**, 10348 (1998).

85. A. D. Becke, *J. Chem. Phys.*, **98**, 5648 (1993).

86. J. B. Forseman and A. Frisch, *Exploring Chemistry with Electronic Structure Methods,* Gaussian Inc., Pittsburgh, PA, 1996.

87. D. L. Bunker, *J. Chem. Phys.*, **37**, 393 (1962).

88. N. C. Blais and D. L. Bunker, *J. Chem. Phys.,* **37**, 2713 (1962).

89. D. L. Bunker, *Method. Comput. Phys.,* **10**, 287 (1971).

90. D. L. Bunker and M. D. Pattengill, *J. Chem. Phys.,* **53**, 3041 (1970).

91. W. J. Lemon and W. L. Hase, *J. Phys. Chem.*, **91**, 1596 (1987).

92. A. J. C. Varandas, *J. Chem. Phys.*, **105**, 3524 (1996).

93. A. J. C. Varandas, *J. Chem. Phys.*, **107**, 867 (1997).

94. F. E. Budenholzer and Y. Tsau, *J. Phys. A,* **102**, 947 (1998).

95. T. G. Wei and R. E. Wyatt, *J. Phys. Chem.,* **97**, 13580 (1993).

96. P. M. Agrawal, D. L. Thompson and L. M. Raff, *J. Chem. Phys.,* **88**, 5948 (1988).

97. B. G. Sumpter and D. L. Thompson, *J. Chem. Phys.,* **88**, 6889 (1988).

98. T. D. Sewell and D. L. Thompson, *J. Chem. Phys.,* **93**, 4077 (1990).

99. S. Nordholm, G. Nymann, H. W. Schranz, *J. Chem. Phys.*, **81**, 2572 (1977).

100. G. Nyman, S. Nordholm, and W. Schranz, *J. Chem. Phys.*, **93**, 6767 (1990).

101. H. Goldstein, *Classical Mechanics*, 2 ed. (Addison-Wesley Publishing Co. Reading, MA, 1981).

102. C. M. Bennett, Unpublished work on IVR in nitromethane and TNAZ indicate that at energy ranges between 250 – 600 kcal/mol NO_2 dissociation is dominated by

modes that provide energy to the R-NO_2 bond. In TNAZ this occurs predominantly through NO bond stretching at the R-NO_2 site and NO_2 angle bending. Low frequency modes tended to contribute equally to torsion and wagging modes.

103. GenDyn code Oklahoma State University.

104. Y. Oyumi, T. B. Brill, A. L. Rheingold, and T. M. Haller, *J. Phys Chem.,* **89**, 4317 (1985).

105. D. C. Sorescu, B. M. Rice and D. L. Thompson, J. Phys. Chem. B **102**, 948 (1998).

106. D. C. Sorescu, B. M. Rice and D. L. Thompson, J. Phys. Chem. A **102**, 8386 (1998).

107. T. D. Sewell and D. L. Thompson, *J. Phys. Chem.,* **95**, 6228 (1991).

108. C. M. Aubuchon, K. D. Rector, W. Holmes, and M. D. Fayer, *Chem. Phys. Lett.*, **299**, 84 (1999).

109. Y. Qin, D. L. Thompson, *J. Chem. Phys.,* 1992 (1992).

110. C. N. Hinshelwood, *Proc. Royal Chem. Soc. A,* **113**, 230 (1927).

111. F. A. Lindemann, *Trans. Faraday Soc.*, **17**, 588 (1922).

112. T. D. Sewell, C. M. Bennett, *J. Appl. Phys.*, **88**, 88 (2000).

113. E. B. Wilson Jr., J. C. Decius, P. C. Cross, *Molecular Vibrations The Theory of Infrared and Raman Vibrational Spectra*, Dover, New York, 1980.

114. Y. Oyumi, T. B. Brill, A. L. Rheingold, T. M. Haller, *J. Phys. Chem.*, **89**, 4317, (1985).

VITA

Carl Mahlon Bennett

Candidate for the Degree of

Doctor of Philosophy

Thesis: ANISOTROPIC ELASTIC MODULI FOR CRYSTALLINE HEXAHYDRO-1,3,5-TRINITRO-1,3,5-TRIAZINE FROM MONTE CARLO CALCULATIONS & MOLECULAR DYNAMIC SIMULATIONS OF THE UNIMOLECULAR DISSOCIATION OF 1,3,3-TRINITROAZETIDINE

Major Field: Chemistry

Biographical:

Personal Data: Born in Anchorage, Alaska on January 19, 1971, the son of Gary M. and Dianne L. Bennett (Colton).

Education: Graduated from Saugus High School, Saugus, California in June 1989; attended the University of Arkansas, Fayetteville, Arkansas from August 1989 to December 1990; received Associates of Science degree and a Bachelor of Science degree in Chemistry with a minor in Physics from Cameron University, Lawton, Oklahoma in December 1993 and May 1995 respectively. Completed the Requirements for the Doctor of Philosophy degree at Oklahoma State University in July 2007.

Experience: Employed by Oklahoma State University as a graduate research assistant and teaching assistant 1995 to 2000. Employed by Los Alamos National Laboratory as a graduate research assistant in 1998.

Professional Memberships: American Chemical Society.

Name: Carl Mahlon Bennett Date of Degree: July, 2007

Institution: Oklahoma State University Location: Stillwater, Oklahoma

Title of Study: ANISOTROPIC ELASTIC MODULI FOR CRYSTALLINE HEXAHYDRO-1,3,5-TRINITRO-1,3,5-TRIAZINE FROM MONTE CARLO CALCULATIONS & MOLECULAR DYNAMIC SIMULATIONS OF THE UNIMOLECULAR DISSOCIATION OF 1,3,3-TRINITROAZETIDINE

Pages in Study: 98 Candidate for the Degree of Doctor of Philosophy

Major Field: Chemistry

Scope and Method of Study: The purpose of this work was two fold. First to determine an efficient means by which to determine the elastic tensor from fluctuation data, specifically, data from Monte Carlo molecular dynamics simulations. The scope focused on the representative high explosive hexahydro-1,3,5-trinitro-1,3,5-triazine (RDX) for the test case of other high explosive grains. The hope is to apply this technique to aid in the mesomechanical and atomistic methods and model of plastic bonded explosives. The second purpose was to model, through classical molecular dynamics, the unimolecular dissociation of 1,3,3-trinitroazetidine (TNAZ) using *ab initio* calculations and experimental data.

Findings and Conclusions: The elastic tensor for RDX was found to be in good agreement with expected results when rigid molecule Monte Carlo molecular dynamics simulations were used. The computed rate of unimolecular dissociation of TNAZ was found to be within the experimental error. The system was found to be statistical.

ADVISER'S APPROVAL: Lionel M. Raff